Anisotropy, multivalency and flexibility-induced effects in colloidal systems

Verweij, R.W.

6 Conformations and diffusion of flexibly-linked colloidal chains

For biologically relevant macromolecules such as intrinsically disordered proteins, internal degrees of freedom that allow for shape changes have a large influence on both the motion and function of the compound. A detailed understanding of the effect of flexibility is needed in order to explain their behavior. Here, we study a model system of freely-jointed chains of three to six colloidal spheres, using both simulations and experiments. We find that in spite of their short lengths, their conformational statistics are well described by two-dimensional Flory theory, while their average translational and rotational diffusivity follow the Kirkwood-Riseman scaling. Their maximum flexibility does not depend on the length of the chain, but is determined by the near-wall in-plane translational diffusion coefficient of an individual sphere. Furthermore, we uncover shape-dependent effects in the short-time diffusivity of colloidal tetramer chains, as well as nonzero couplings between the different diffusive modes. Our findings may have implications for understanding both the diffusive behavior and the most likely conformations of macromolecular systems in biology and industry, such as proteins, polymers, single-stranded DNA and other chain-like molecules.

6.1 Introduction

For biologically relevant (macro)molecules, internal degrees of freedom that allow for shape changes have a large influence on both the motion and function of the compound.[100–104] Examples of flexible systems found in nature include bio-polymers such as DNA and transfer RNA,[251] antibodies[101,103,253,254] and intrinsically disordered proteins (IDPs).[252,282] IDPs in particular display large shape changes, due to unstructured (and therefore flexible) regions of small hydrophilic units that typically function as linkers between more structured domains. These are involved in important cellular processes such as signaling and transcription. Additionally, they are often involved in disease-related gene truncations or translocations. The coupled binding and folding of these flexible regions lead to a large number of possible interactions within the same set of proteins.[282] Even for more rigid proteins, shape changes can be an important factor, for example in protein breathing, that involves slow collective movements of larger secondary structures.[283] Therefore, quantitative knowledge of structural flexibility is necessary to understand the transport properties and function of flexible biopolymers and proteins.[261]

Measuring molecular shape changes calls for single-molecule techniques with a simultaneously high spatial and temporal resolution. As a simpler alternative, colloidal particles have been widely used as model systems for (macro)molecular structures since the early 20th century,[18,19,284] because of their unique combination of microscopic size and sensitivity to thermal fluctuations. Although colloidal particles are frequently used as model systems, the study of colloidal particles is interesting in its own right, as colloids can in principle form the building blocks of materials with novel properties, such as photonic bandgap materials.[2] Colloidal structures of reconfigurable shape are expected to aid in the assembly of these structures, because they allow the formed materials to quickly relax towards their thermodynamic equilibrium configuration, thereby mitigating "hit-and-stick" equilibration issues.[77,196] In addition, they could provide ways to build switchable materials.[285]

While the Brownian motion of rigid colloids of various shapes has been extensively studied, for example for ellipsoids,[91,95,96] boomerangs,[14,97,98] and clusters,[12,13] most compounds found in nature show some degree of flexibility, which may affect their transport properties. It was proposed to calculate their diffusive properties in an approximate way, by treating the structure as an (instantaneously) rigid body and take the ensemble average of all possible 'snapshots' of conformations, the so called rigid body approximation.[101,264,286,287] However, the accuracy of this approximation is as of yet unclear: importantly, deviations between this approximation and the real transport properties can become larger as function of the flexibility of the molecule.[288]

Recently, we have studied both numerically and experimentally the effect of segmental flexibility[244] in a simple model system consisting of a freely-jointed chain of three spherical colloidal particles, also called trimers or trumbbells.[107,262] This was made possible for the first time thanks to the development of colloidal structures with freely-jointed bonds.[110] Similar to rigid particles, we found that shape affects the diffusive motion of the colloid at short timescales and that displacements are larger in directions that correspond to smaller hydrodynamic drag. By comparing our flexible trimers to rigid ones, we found that the flexibility of the trimers led to a higher translational diffusion coefficient. Furthermore, we uncovered a Brownian quasiscallop mode, where diffusive motion is coupled to Brownian shape changes. At longer timescales, in addition to the rotational diffusion time, an analogous conformational diffusion time governs the relaxation of the diffusive motion, unique to flexible assemblies.[244] These effects taken together show that the rigid body approximation is not sufficient to model the rich behavior of flexible objects. However, in the case of long polymer chains, Kirkwood-Riseman theory,[286] which is based on the rigid body approximation, is able to at least describe equilibrium properties such as the average translational diffusion coefficient.[289] This is attractive because, if accurate, it would provide a simple and quick way to calculate the equilibrium long time diffusion coefficients typically measured in light scattering experiments.

Here, we study flexible chains of three to six particles using both experiments and simulations. Conceptually, the longer chains most resemble a flexible polymer, modeled by beads on a chain, while the shorter chains are expected to show devi-

ations from predictions based on polymer theory. We set out to test to what extent the conformations of our bead chains can be described by polymer theory and to what extent their equilibrium diffusivity can be described by simple scalings such as the Kirkwood-Riseman model. First, we analyze their conformational free energy in several different ways and compare our findings to two-dimensional Flory theory. Then, we study the shape-dependent short-time diffusivity of the trimer and tetramer chains and calculate the full diffusion tensor as function of instantaneous shape. By also determining the shape-averaged translational diffusivity, rotational diffusivity and flexibility for chains of three to six spheres, we show how these scale as function of chain length. Overall, we find a good agreement between the experimental measurement and the simulations, except for translational diffusivity. In that case, we hypothesize that the difference in surface slip in the experiments, where the substrate has a finite slip length due to the hydrogel surface, and simulations, where we use a no-slip boundary condition, lead to the higher translational diffusivity in the experiments. We hope our work aids the study of diffusivity of flexible objects found in complex mixtures relevant in, for example, the cosmetic, pharmaceutical and food industries, as well as in biological systems. Our findings may have implications for understanding both the diffusive behavior and the most likely conformations of macromolecular systems in biology and industry, such as polymers, single-stranded DNA and other chain-like molecules.

6.2 Materials and Methods

6.2.1 Experimental

Flexible chains of colloid-supported lipid bilayers (CSLBs) were prepared as described in previous work,[85,110,112,242] specifically, we followed the exact same procedure as in Chapter 5[244] and used silica particles of two different radii to test the generality of our findings. We now briefly summarize the experimental procedure from Chapter 5.[244]

The CSLBs consisting of $(2.12 \pm 0.06)\,\mu m$ silica particles were prepared as described in our recent works.[242,244] Briefly, the particles were coated with a fluid lipid bilayer by deposition and rupture of small unilamellar vesicles consisting of 98.8 mol % of the phospholipid DOPC ((Δ9-Cis)-1,2-dioleoyl-sn-glycero-3-phosphocholine), 1 mol % of the lipopolymer DOPE-PEG(2000) (1,2-dioleoyl-sn-glycero-3-phosphoethanolamine-N-[methoxy(polyethylene glycol)-2000]) and 0.2 mol % of the fluorescently-labeled lipids TopFluor-Cholesterol (3-(dipyrromethene boron difluoride)-24-norcholesterol) or DOPE-Rhodamine (1,2-dioleoyl-sn-glycero-3-phosphoethanolamine-N-(lissaminerhodamine B sulfonyl)). The bilayer coating was performed in a buffer at pH 7.4 containing 50 mM sodium chloride (NaCl) and 10 mM 4-(2-Hydroxyethyl)-1-piperazineethanesulfonic acid (HEPES). We added double-stranded DNA (of respectively strands DS-H-A and DS-H-B, see Table A.1) with an 11 base pair long sticky end and a double stearyl anchor, which inserts itself into the bilayer via hydrophobic interactions (see Figure 6.1a, left panel). The sticky

end of strand DS-H-A is complementary to the sticky end of strand DS-H-B, which allows them to act as linkers. Self-assembly experiments were performed in a different buffer of pH 7.4, containing 200 mM NaCl and 10 mM HEPES. Chains of 2.12 μm CSLBs were formed by self-assembly in a sample holder made of polyacrylamide (PAA) coated cover glass.[244] Confocal microscopy images of the coated particles are shown in Figure 6.2a, for chain lengths of $n = 3$ to 6 particles.

Additionally, we analyzed chains of (1.93 ± 0.05) μm CSLBs, with silica particles purchased from Microparticles GmbH (product code SiO_2−R-B1072). We followed the same protocol with two minor modifications: first, the lipid composition was 91.2 mol % DOPC, 8.7 mol % DOPE-PEG(2000) and 0.1 mol % DOPE-Fluorescein. Second, we added double-stranded DNA with a self-complementary 12 base pair sticky end (i.e. a palindromic sequence) and a cholesterol anchor that inserts itself into the lipid bilayer due to hydrophobic interactions (see Table A.1, strands PA-A and PA-B). To image the 1.93 μm CSLBs we used a flow cell coated with poly(2-hydroxyethyl acrylate) (pHEA) polymers.[244] Self-assembly experiments were performed in a buffer of pH 7.4, containing 50 mM NaCl and 10 mM HEPES.

6.2.2 Microscopy

Chains were imaged for at least 5 min (frame rates between 5 and 19 fps) at room temperature using an inverted confocal microscope (Nikon Eclipse Ti-E) equipped with a Nikon A1R confocal scanhead with galvano and resonant scanning mirrors. A 60× water immersion objective (NA=1.2) was used. 488 and 561 nm lasers were used to excite, respectively, the Fluorescein or TopFluor and Rhodamine dyes. Laser emission passed through a quarter wave plate to avoid polarization of the dyes and the emitted light was separated by using $500 - 550$ nm and $565 - 625$ nm filters.

To complement the data obtained from self-assembled chains, we used optical tweezers to assemble specific chain lengths. Briefly, we employed a homemade optical setup consisting of a highly focused trapping laser manufactured by Laser QUANTUM (1064 nm wavelength). The laser beam entered the confocal microscope through the fluorescent port, after first passing through a beam expander and a near-infrared shortpass filter. The same objective was used for imaging and to focus the trapping laser beam. During the trapping, the quarter wave plate was removed from the light path.

Particle positions were tracked using a custom algorithm[242] available in TrackPy by using the `locate_brightfield_ring` function[188] or using a least-square fit of a Mie scattering based model implemented in HoloPy.[186] Both methods agree to an accuracy of at least 1 px, however we have found that the Mie scattering based model is more robust for tracking multiple particles in close proximity to each other. For all analysis, we only selected clusters that showed all bond angles during the measurement time, experienced no drift and were not stuck to the substrate. An overview of the total number of measurements, the total duration and the total number of frames per chain length is shown in Table 6.1.

Table 6.1: Overview of the amount of measurements, the total duration and the total number of frames per chain length, for the experimental and simulated data.

n	**Measurements**		**Total length [min]**		**Total frames**	
	Exp.	Sim.	Exp.	Sim.	Exp.	Sim.
3	30	30	275	900	9.3×10^4	3.8×10^7
4	69	50	305	1500	2.5×10^5	6.4×10^7
5	13	20	75	600	4.7×10^4	2.5×10^7
6	5	20	41	600	4.1×10^4	2.5×10^7

Table 6.2: **Permutation data.** For all chain lengths n, we generated the $P(N_\theta, n-2)$ configurations obtained by permuting all possible combinations of opening angles. Interpenetrating configurations, which are forbidden due to short-range repulsive forces between particles, were removed from this permutation data and the percentages of these configurations relative to the total number of configurations between 60 and 300 deg, as well as between 0 and 360 deg (fully freely-jointed case) are shown.

n	$\delta\theta$ [deg]	$P(N_\theta, n-2)$	**Interpen. [%]** (60-300 deg)	**Interpen. [%]** (0-360 deg)
3	0.01	2.4×10^4	0	33.3
4	0.04	3.6×10^7	6.3	58.3
5	0.50	1.1×10^8	14.0	74.5
6	2.00	2.0×10^8	21.9	84.7

6.2.3 Simulations

We have performed Brownian dynamics simulations with hydrodynamic interactions following the method outlined in Sprinkle et al. [290] using the open-source RigidMultiblobsWall package.[291] Hydrodynamic interactions are calculated using the Stokes equations with no-slip boundary conditions. The hydrodynamic mobility matrix is approximated using the Rotne-Prager-Blake (RPB) tensor,[35] which is a modified form of the Rotne-Prager-Yamakawa (RPY) tensor[34,275,292] and accounts for a bottom wall, which is unbounded in the transverse directions. These corrections to the RPY tensor are combined with the overlap corrections described in Wajnryb et al. [292] to prevent particle-particle and particle-wall overlap. The RPB mobility inaccurately describes near-field hydrodynamic interactions and therefore breaks down for small separation distances. This can be overcome by adding a local pairwise lubrication correction to the RPB resistance matrix as described in detail in Sprinkle et al. [290] Based on the full lubrication-corrected hydrodynamic mobility matrix, the Ito overdamped Langevin equation is solved to describe the effect of thermal fluctuations.

We include a gravitational force on the particles to confine them to diffuse close to the bottom wall, as in the experiments. Inter-particle bonds are modeled by harmonic springs of stiffness $1000 k_B T/R^2$ and equilibrium length $2R$, where $R = 1.06\,\mu\text{m}$ is the particle radius. The bond angle is not restricted. We set the temperature $T = 298\,\text{K}$, the viscosity of the fluid $\eta = 8.9 \times 10^{-4}\,\text{Pa s}$, the gravitational acceleration $g = 9.81\,\text{m s}^{-2}$, the particle mass $m_p = 9.5 \times 10^{-15}\,\text{kg}$ (by assuming a particle density of $1900\,\text{kg m}^{-3}$) and the simulation timestep $\Delta t = 1.42\,\text{ms}$. For the firm potential that prevents overlap, we use a strength of $4 k_B T$ and a cutoff distance $\delta_{\text{cut}} = 10^{-2}$.[290,293] We initialized the particle chains in a linear configuration (all opening angles 180°). Then, these initial configurations were randomized by running the integration for a simulated time of 60 s prior to saving the configurations, to ensure a proper equilibration of the particle positions, bond lengths, velocities and opening angles. The particle positions were saved every 8 simulation steps to obtain a final framerate of approximately 90 fps. An overview of the total number of simulations, the total duration and the total number of saved frames per chain length is shown in Table 6.1.

For comparison to the simulated and experimental data, we generated data in which the chains are completely non-interacting and freely-jointed up to steric exclusions in the following manner: we generated all $(n-2)$-permutations of the N_θ opening angles θ_i, which gives a total number of $P(N_\theta, n-2) = N_\theta!/(N_\theta - (n-2))!$ combinations of θ_i. Here, the number of opening angles is $N_\theta = (360 - 2 \times 60)/(\delta\theta)$, where $\delta\theta$ denotes the bin width. Then, we removed those combinations that are forbidden because of steric exclusions between particles, resulting in the final allowed combinations, which we call "permutation data". In Table 6.2, we show the bin widths $\delta\theta$ for each n, as well as the total number of generated permutations $P(N_\theta, n-2)$. The percentage of permutations that was removed due to steric exclusions is shown, as well as the total number of configurations that would result in interpenetrating particles for the completely freely-jointed case, where θ can vary between 0 and 360 deg.

6.2.4 Data analysis

For all fits reported in this work, used a Bayesian method to find an estimate of the posterior probability distribution, by using an Affine Invariant Markov chain Monte Carlo (MCMC) Ensemble sampler method as implemented in the Python packages `lmfit`[246] and `emcee`.[207] This allowed us to obtain accurate estimates of the error and the maximum likelihood estimate (MLE) of the parameters. Parameter values were initialized using a standard least-square fit, appropriate bounds on the parameter values were implemented as priors. We estimated the autocorrelation time τ_{acor} of the MCMC chain using the built-in methods and ran the analysis for at least $100\tau_{\text{acor}}$ steps, where we discarded the first $2\tau_{\text{acor}}$ steps (corresponding to a burnin phase) and subsequently used every other $\tau_{\text{acor}}/2$ steps (known as thinning). We used 500 independent chains (or walkers). The reported values correspond to the maximum likelihood estimate of the resulting MCMC chains, the reported uncertainties correspond to the 16$^{\text{th}}$ and 84$^{\text{th}}$ percentiles of the obtained posterior probability distribution.

6.2.5 Diffusion tensor analysis

Definition of the diffusion tensor

We determined the short-time diffusivity of the clusters, both as function of their instantaneous shape, as well as averaged over all possible configurations. Because the chains are sedimented to the bottom substrate, we consider only the quasi-2D, in-plane diffusivity. For the flexible trimers, we followed the methods outlined in Chapter 5.[244] For the flexible tetramer chains, we calculated a 5×5 diffusion tensor, where the four degrees of freedom correspond to translational diffusivity in x and y, rotational diffusivity and the flexibilities of the tetramer, which are described by the diffusivities of the opening angles θ_1, θ_2. Specifically, the x- and y-directions are schematically shown for one configuration in Figure 6.1b and defined by Equation 6.4. The rotation angle used for determining the rotational diffusivity is indicated in Figure 6.1b and is the angle of the $x(\tau)$ relative to $x(\tau = 0)$, i.e. the angle of the body-centered x-axis of the current frame relative to the body-centered x-axis of the reference frame at $\tau = 0$. The flexibilities are calculated from the mean-squared displacements of the opening angles θ_1, θ_2, which are depicted in Figure 6.1b. θ_1 is defined in such a way that it is always less than or equal to 180 deg and this defines how we assign the magnitude of θ_2, specifically, whether it is acute or obtuse.

The diffusion tensor elements of the tetramer chains were determined analogously to the trimers.[244] Briefly, for each pair of frames, we determined the initial shape of the chain, which is determined by θ_1, θ_2. The short time diffusion tensor is then calculated from the trajectories in the following way:

$$\boldsymbol{D}[ij](\theta_1, \theta_2) \equiv \frac{1}{2} \frac{\partial \langle \Delta i(\theta_1, \theta_2) \Delta j(\theta_1, \theta_2) \rangle_\tau}{\partial \tau}, \tag{6.1}$$

with τ the lag time between frames, $\langle \cdots \rangle_\tau$ denotes a time average over all pairs of frames τ apart and $\Delta i(\theta_1, \theta_2) = i(\theta_1, \theta_2, t + \tau) - i(\theta_1, \theta_2, t)$ is the displacement of the i-th diffusion tensor element, which depends on the instantaneous shape given by θ_1, θ_2. The average diffusion tensor elements $\boldsymbol{D}[ij]$ were obtained by fitting the overall slope of the mean (squared) displacements as a function of lag time τ. We considered lag times up to 0.17 s, given by the frame rate of the experimental data. We only considered trajectories where the variation in θ_1, θ_2 did not exceed the edges of the bin describing the initial shape. Then, we calculated the diffusion tensor elements separately for each initial shape. For fitting the slopes, we used a MCMC sampling method described in Section 6.2.4, where we used a linear model without an offset. For longer chains, we only considered the shape-averaged, quasi-2D translational diffusion coefficient D_T, which corresponds to in-plane diffusivity above the wall. Additionally, we determined the rotational diffusion coefficient $D[\alpha\alpha]$ from the mean squared angular displacement of the x-axis (defined in Equation 6.4, see Figure 6.1b for a schematic depiction), which describes the rotational diffusivity around an axis perpendicular to the substrate. Finally, we determine the overall cluster flexibility $D[\boldsymbol{\theta\theta}]$ by calculating the mean squared displacements of the $(n-2)$ opening angles

θ_i as follows:

$$\langle |\Delta\boldsymbol{\theta}|^2 \rangle = \langle |(\Delta\theta_1, \ldots, \Delta\theta_{n-2})|^2 \rangle, \tag{6.2}$$

so that the flexibility $D[\boldsymbol{\theta}\boldsymbol{\theta}]$ is given by

$$\langle |\Delta\boldsymbol{\theta}|^2 \rangle = 2(n-2)D[\boldsymbol{\theta}\boldsymbol{\theta}]t, \tag{6.3}$$

analogously to the other diffusion tensor elements.

The influence of the tracking point

As tracking point, we considered the center of mass (c.m.) and the center of diffusion (c.d.), because the choice of origin is expected to affect the magnitude of the diffusion tensor.[105,269] The c.d. was calculated from $\boldsymbol{A}_{ij}$ defined by Equation 2.16 of Cichocki et al.[269] using the RPB tensor[35] with lubrication corrections as the inter-particle mobility matrix $\boldsymbol{\mu}_{ij}$. This tensor includes wall corrections, as discussed previously in Section 6.2.3. The c.d. was determined from the simulated particle positions, because the height above the bottom wall was not measured experimentally, but is needed to calculate the wall corrections. The direction of the body-centered x- and y-axes was determined as function of the tracking point $\boldsymbol{r}_{t.p.}$, which defines the origin of the body-centered coordinate frame. We define $\boldsymbol{r}_{t.p.} = \rho_1\boldsymbol{r}_1 + \rho_2\boldsymbol{r}_2 + \cdots + \rho_n\boldsymbol{r}_n$, which defines the location of the tracking point as a linear combination of the particle positions (Equation 2.2 and 2.3 of Cichocki et al.[269]). $\boldsymbol{\rho} = (\rho_1, \rho_2, \ldots, \rho_n)$ is a weight vector which determines how much weight is accorded to each particle in the calculation of the tracking point $\boldsymbol{r}_{t.p.}$. As an example, for a trimer, $\boldsymbol{\rho} = (1/n = 1/3, 1/3, 1/3)$ when the tracking point is chosen to be the center of mass.

The direction of the x-axis was chosen as

$$\hat{\boldsymbol{x}} = \pm \left[\frac{\boldsymbol{r}_{t.p.,1} + \cdots + \boldsymbol{r}_{t.p.,s_1}}{\rho_1 + \cdots + \rho_{s_1}} - \frac{\boldsymbol{r}_{t.p.,s_2} + \cdots + \boldsymbol{r}_{t.p.,n}}{\rho_{s_2} + \cdots + \rho_n} \right], \tag{6.4}$$

where $\boldsymbol{r}_{t.p.,i}$ is the i-th coordinate of the tracking point and the bead chain is split into two parts with equal numbers of particles according to

$$\begin{cases} s_1 = s_2 = \lceil \frac{n}{2} \rceil & \text{for odd } n \\ s_1 = \lceil \frac{n}{2} \rceil, s_2 = s_1 + 1 & \text{for even } n \end{cases} \tag{6.5}$$

Note that for a trimer, with the tracking point at the c.m. (i.e. $\boldsymbol{\rho} = (1/3, 1/3, 1/3)$), $\hat{\boldsymbol{x}}$ is parallel to the end-to-end vector, which is the same definition as in our previous work.[244] $\hat{\boldsymbol{y}}$ is then chosen such that $\hat{\boldsymbol{x}}$ and $\hat{\boldsymbol{y}}$ form a right-handed coordinate system, where the direction of $\hat{\boldsymbol{y}}$ is chosen to point away from the central part of the cluster towards the tracking point, i.e. along $\boldsymbol{r}_{t.p.} - \left(\boldsymbol{r}_{s_1} + \boldsymbol{r}_{s_2}\right)/2$. This orientation was determined for every frame, which fixed the orientation of the body-centered coordinate system $\boldsymbol{x}(\tau = 0), \boldsymbol{y}(\tau = 0)$. For subsequent lag times, the direction of $\boldsymbol{y}(\tau)$ was chosen such that $\boldsymbol{y}(\tau = 0) \cdot \boldsymbol{y}(\tau) > 0$, i.e. the direction of $\boldsymbol{y}$ does not change sign. The resulting coordinate system relative to the c.d. is visualized for the tetramer chains in Figure 6.1b and c.

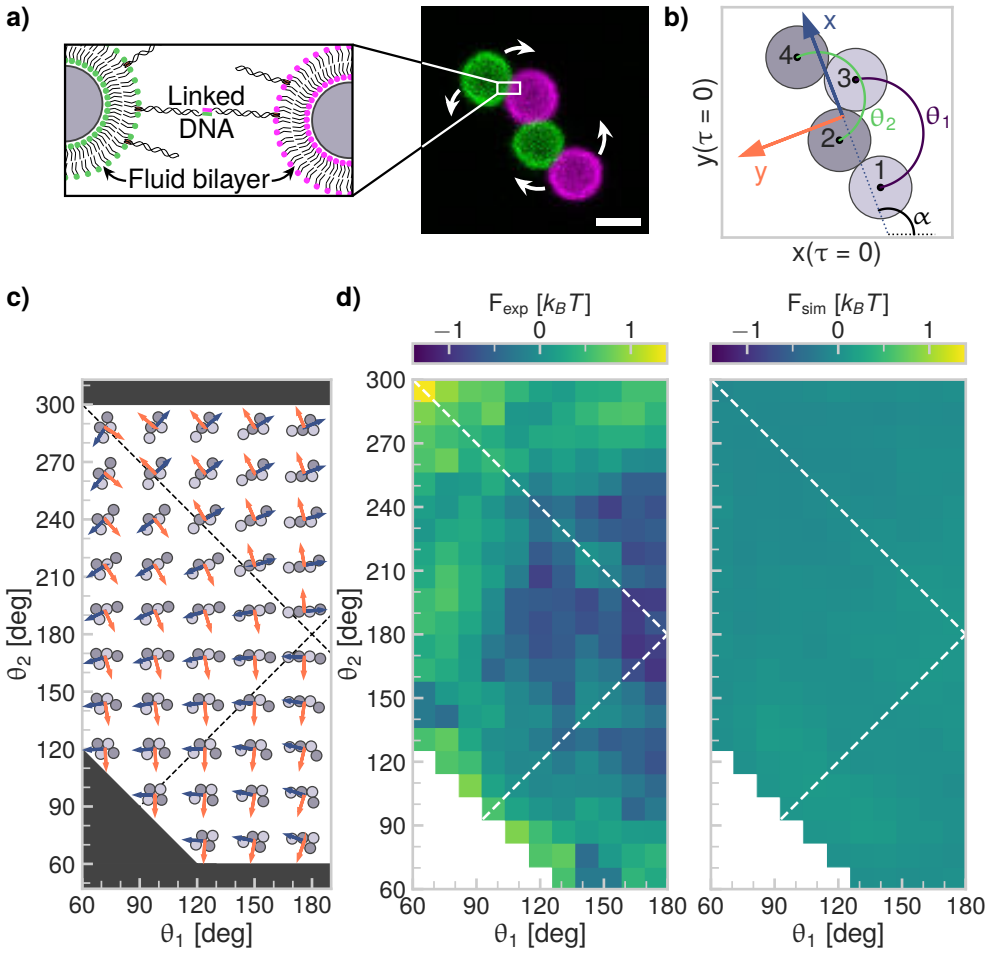

Figure 6.1: **Flexibly linked colloidal tetramers. a)** Flexibly linked colloidal chains are created from DNA functionalized colloid-supported lipid bilayers (CSLBs). The particles are bound by the DNA linkers, which can diffuse in the fluid lipid bilayer, yielding reconfigurable assemblies. Right: Confocal image of a tetramer chain, where the different colors, stemming from fluorescently labeled lipids, indicate the two different particle types that are functionalized with complementary DNA linkers. Scalebar is 2 µm. **b)** The coordinate system used for quantifying the diffusion of tetramer chains, relative to the center of diffusion (see Section 6.2.5). **c)** Schematics of possible configurations for the tetramer, as function of the two opening angles θ_1, θ_2. Some configurations are sterically prohibited because the particles cannot interpenetrate (as indicated by the dark grey area). The dashed lines indicate the two symmetry axes of the opening angles, $\theta_2 = \theta_1$ and $\theta_2 = 360\,\text{deg} - \theta_1$. **d)** The free energy of both experimental (left) and simulated (right) chains of four particles in terms of θ_1, θ_2.

6.3 Results and Discussion

6.3.1 Conformations of flexible chains

Shape as function of the trimer segments

Does a diffusing flexible chain of micron-sized spherical particles have preferred configurations? This is a natural question to ask, because increasing the number of spheres per chain increases the percentage of overlapping configurations (see Table 6.2) and could potentially change the hydrodynamic interactions. We answer this question by considering the free energy of such chains, which were made by the assembly of colloid-supported lipid bilayers (CSLBs).[85,110,112,242,244] These particles are bonded by DNA linkers, which provide specific bonds between the particles. Because the linkers can diffuse in the fluid lipid bilayer, the bonded particles can move with respect to each other (see Figure 6.1a for a schematic). We compared our experimental data to Brownian dynamics simulation data, where hydrodynamic interactions between particles and the substrate are taken into account via the Rotne-Prager-Blake (RPB) tensor,[35] overlap corrections[292] and a local pairwise lubrication correction[290] (see Section 6.2.3 for details).

We analyzed the free energy of clusters of $n = 3$ to 6 particles as function of their conformation using different methods. For a chain of three particles, a trimer, a single parameter, the opening angle θ, can describe the conformations.[244] We have shown before that flexible trimers do not show a preference for any given opening angle and therefore conformation.[242,244] For a chain of four of such particles (see Figure 6.1a for a microscopy image), there are two angles that characterize the shape of the cluster, θ_1 and θ_2, which are the opening angles of the two "trimer segments" (groups of three adjacent, bonded spheres) that make up the chain. The definition of the opening angles is shown in Figure 6.1b. For the tetramer chains, we obtained a 2D-histogram of opening angles for θ_1, θ_2 between 60° to 300°, using the simulated and experimental data. These two internal degrees of freedom lead to a large number of possible chain configurations, as shown in Figure 6.1c. Some configurations are forbidden because of steric exclusions, as indicated by the grey areas. The symmetry lines of the opening angles $\theta_2 = \theta_1$ and $\theta_2 = 360\,\mathrm{deg} - \theta_1$ are indicated as well. The configurations are symmetric around these lines except for the fact that we break this symmetry by choosing which angle to label as θ_1 and which as θ_2, because this has consequences for the orientation of the body centered coordinate system, as shown in Figure 6.1b and defined in Equation 6.4.

From the probability density function calculated from the histogram, we determined the free energy using Boltzmann weighing,

$$\frac{F}{k_B T} = -\ln p + \frac{F_0}{k_B T}, \tag{6.6}$$

where F is the free energy, k_B is the Boltzmann constant, T is the temperature, p is the probability density and F_0 is an arbitrary constant offset to the free energy that

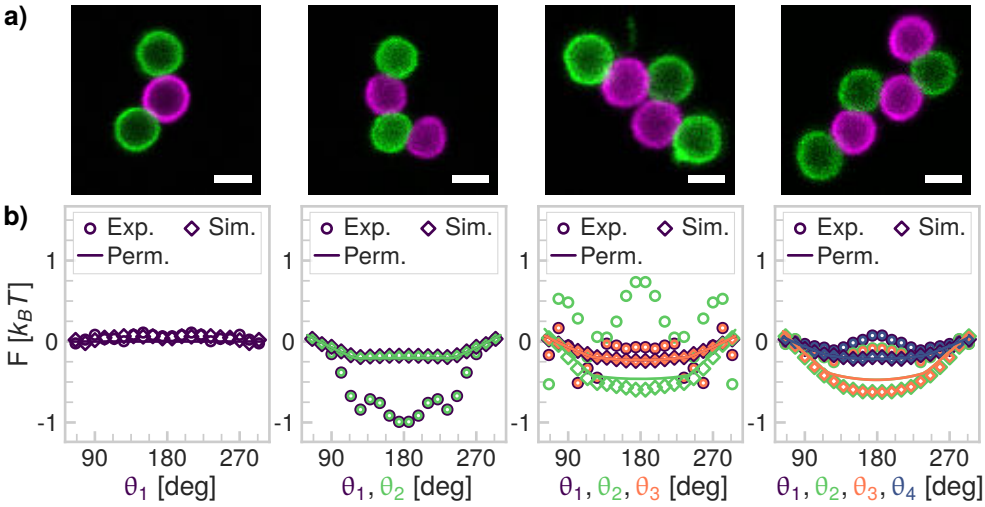

Figure 6.2: **Flexibly-linked colloidal chains. a)** Confocal microscopy images of, left to right, a trimer ($n = 3$), tetramer ($n = 4$), pentamer ($n = 5$) and hexamer ($n = 6$) chain. Scalebars are 2 µm. **b)** The free energy in terms of the opening angles of groups of three particles ("trimer segments"), of, left to right, trimers, tetramers, pentamers and hexamers. The main contribution to the free energy is the configurational entropy of the chains. ∘ Experimental, ⋄ simulated and permutation data (Perm.) are shown, different colors indicate different opening angles.

we have chosen such that the average free energy is equal to zero. Except for steric restrictions and hydrodynamic interactions, we expect inter-particle interactions to be weak. Therefore, we hypothesize that there are mainly entropic contributions to the free energy and that enthalpic contributions are small. The resulting free energy is shown in Figure 6.1d. Like flexible trimers,[242,244] chains of four particles are freely-jointed, as evidenced by the fact that differences in their free energy as function of opening angles θ_1, θ_2 are on the order of $1\,k_BT$ in Figure 6.1d in the experiments and below $0.1\,k_BT$ in the simulations. Differences smaller than or comparable to the thermal energy are difficult to measure experimentally and are of limited physical relevance. Therefore, we conclude that there is no appreciable preference for any given conformation and the tetramer chains are thus freely-jointed. We use the term "freely-jointed" in the sense that the chains are free to move without any preferred state, up to steric exclusions stemming from short-range repulsions between the particles that prevent them from interpenetrating.

Increasing the number of beads in the chain increases the percentage of sterically inaccessible configurations (see Table 6.2) and could potentially alter the hydrodynamic interactions. To answer whether these effects lead to preferred configurations, we study chains consisting of n=3 to 6 particles, as shown in confocal microscopy images in Figure 6.2a. Because visualization as a joined histogram becomes increas-

ingly complex as the chain length increases, we first consider the free energy of their separate $(n-2)$ opening angles, as shown in Figure 6.2b. First, we obtained probability density functions of their $n-2$ opening angles θ_i, where θ_i is the i-th opening angle, as defined in Figure 6.3a, analogously to the choice of opening angles θ_1, θ_2 in Figure 6.1b. In other words, we consider the free energy as function of the opening angles of the trimer segments of the chains. We label the first particle with $i = 1$ and number the rest of the chain consecutively. Because there are two choices for the first particle on either end of the chain, which opening angle is labeled by the first index is not unique. Therefore, we include both choices in our analysis. Additionally, we include both choices of defining θ_1 as either obtuse or acute and then use the same convention for the other opening angles.

Whilst a trimer (n=3) shows no preference for any specific configuration,[242,244] the tetramer chains do show a small preference for straight opening angles, as evidenced by the differences in free energy between compact opening angles and straight opening angles in Figure 6.2b. These deviations are largest in the experimental data, but also present to a lesser degree in the simulation data and the permutation data. The deviations in the simulated and permutation data can only stem from steric exclusions, which cause some configurations to be inaccessible: for a tetramer chain, angles below 60 deg or above 300 deg and combinations where $\theta_1 + \theta_2 < 180$ deg or $\theta_1 + \theta_2 > 540$ deg are not possible due to steric restrictions. Seeing that we have strong indications that the bond angles are freely-jointed up to steric exclusions in the simulated and permutation data, we believe that the larger deviations in the experimental data in Figure 6.1d and Figure 6.2b, compared to the simulation and permutation data, are mostly caused by experimental noise. This can be mitigated by collecting more data, however, the amount of data needed to characterize the free energy in sufficient angular detail is very large (see Table 6.1 for a comparison between the amount of simulated and experimental data). Because the experimental deviations are below the thermal energy, we conclude that also in the experiments, there is no preference for any of the sterically allowed configurations.

For the free energy of the pentamer chains in Figure 6.2b, we observe some larger deviations of the experimental data compared to the permutation and simulated data. Specifically, the central angle seems to show a preference for closed angles, as evidenced by the lower free energy for $\theta_2 = 60$ deg and 300 deg. However, the difference between the compact angles and the stretched angles is small, i.e. less than $1.5\,k_BT$. Considering the free energy of the hexamer chains, we observe that the distribution of the outer opening angles θ_1, θ_4 is flatter than the distribution of the inner opening angles θ_2, θ_3, especially in the simulated and permutation data. Interestingly, there is a clear trend in the free energy of flexible chains, going from a flat free energy for $n = 3$ to a free energy that shows a minimum at 180 deg and becomes increasingly smooth as the chain length increases. The location of the minimum and the good agreement with the permutation data show that the deviations from a flat free energy most likely stem from the steric exclusions at compact opening angles.

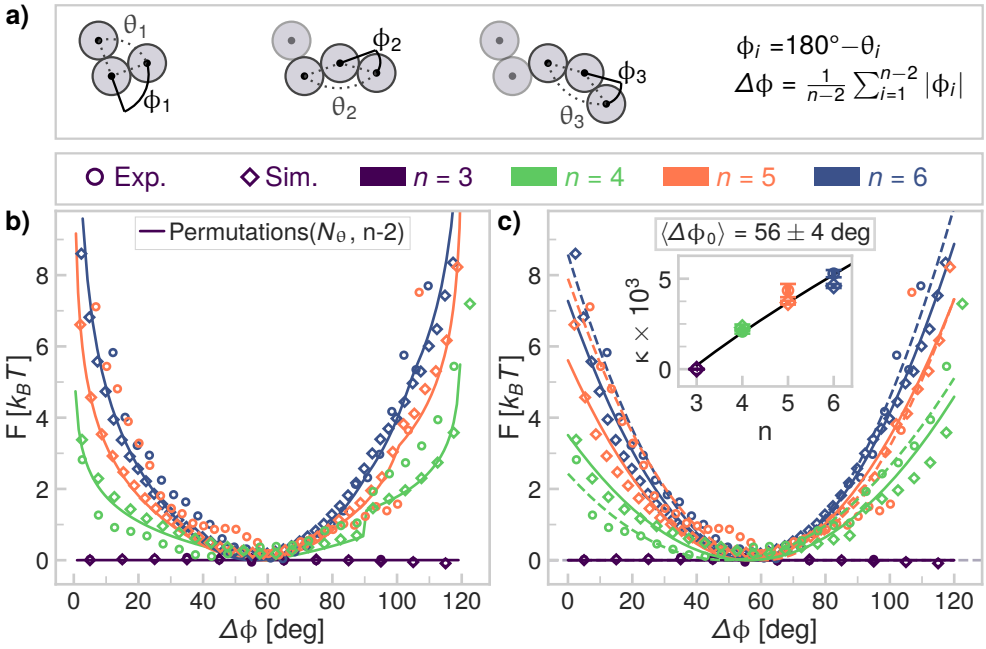

Figure 6.3: **Average bending angle of flexible colloidal chains. a)** Top: we define a quantity $\Delta\phi$ which measures how much the chain shape deviates from a straight line. Bottom: Markers for the ∘ experimental and ⋄ simulated data, together with the color coding legend for the different chain lengths n, as used in panels b and c are shown above those panels. **b)** Comparison between the free energy calculated for experimental, simulated and the $P(N_\theta, n-2)$ permutation data, as function of $\Delta\phi$. **c)** Free energy in terms of $\Delta\phi$ and fit of Equation 6.8 (fit values shown in the insets). Additionally, we fit Equation 6.9 to determine the scaling of κ as function of n, as shown in the inset.

Shape as function of the average bending angle $\Delta\phi$

So far, we have considered the free energy in terms of the individual opening angles or trimer segments. To analyze the overall shapes these colloidal chains can adopt in more detail, we define the average bending angle $\Delta\phi$, as shown schematically in Figure 6.3a. This allows us to study the overall shape of the chains by collapsing the $(n-2)$-dimensional description of the shape in terms of opening angle, onto a single measure of chain shape. We converted all pairs of opening angles to the single average bending angle,

$$\Delta\phi = \frac{1}{n-2}\sum_{i=1}^{n-2}\left|\phi_i\right|, \tag{6.7}$$

as defined in Figure 6.3a. We then obtained the probability density function in terms of $\Delta\phi$ and converted this to a free energy using Equation 6.6, as shown in Figure 6.3b. By taking this approach, we find that as the number of particles n is increased, a preferred average bending angle arises at $\Delta\phi_0 = (56 \pm 4)\,\mathrm{deg}$, close to the average of 60 deg between no bending (0 deg) and maximal bending (120 deg), for the experimental, simulated and permutation data. Additionally, the free energy profiles of all chain lengths show the same shape, where the difference in free energy between the most likely and least likely configurations increases as the chain length increases.

The free energy in terms of $\Delta\phi$ effectively quantifies the average bending angle, or put simply, bending free energy, which is expected to be harmonic based on the worm like chain model.[294] We fitted a harmonic potential V to the resulting free energy of the form

$$V = \frac{\kappa}{2b}\left(\Delta\phi - \Delta\phi_0\right)^2, \tag{6.8}$$

with fit parameters κ the stiffness of the potential well in units of $\mathrm{k_BT/deg^2}$ and $\Delta\phi_0$ the center of the potential well in deg, as shown in Figure 6.3c. We find that the potential well stiffness κ increases as the number of particles increases (see second inset of Figure 6.3c) as predicted by polymer theory.[294] Namely, we fit

$$\kappa = \alpha\frac{b}{4}(n-1)^{\nu} - \kappa_0, \tag{6.9}$$

where $\kappa_0 = (5.1 \pm 0.7) \times 10^{-3}\,\mathrm{k_BT/deg^2}$ fixes the value of κ for $n = 3$ and $\alpha = (13 \pm 1) \times 10^{-3}\,\mathrm{k_BT/deg^2}$ is a positive constant. We added κ_0 to the model described by Wiggins and Nelson[294] to ensure that $\kappa = 0$ for $n = 3$ as we observe from our data. Additionally, we added the scaling parameter α to ensure the proper magnitude of κ. Clearly, for $n = 3$, the chain is freely-jointed and therefore $\kappa = 0$. For larger chains, the probability to observe deviations from a straight configuration decreases as the number of configurations with steric exclusions increases (see Table 6.2), as is evidenced by the agreement between the permutation, the experimental and the simulated data in Figure 6.3b. Therefore, the bending stiffness that we measure is an effective parameter, purely arising from these steric exclusions.

Distribution of the end-to-end distance and radius of gyration: a comparison with polymer theory

We now compare the behavior of our flexibly linked particle chains to predictions from two-dimensional Flory theory for self-avoiding polymers. We are interested in first testing whether our colloidal chains show the same behavior as long polymers in terms of RMS end-to-end distance and radius of gyration, as was shown for chains of flexibly linked oil droplets.[194] Then, we compare the distributions of the end-to-end distance and radius of gyration of the colloidal chains to predictions from polymer theory, to elucidate where finite-size effects start to play a dominant role in the configurational free energy of chain-like molecules. In Figures 6.4–6.5, we have compared

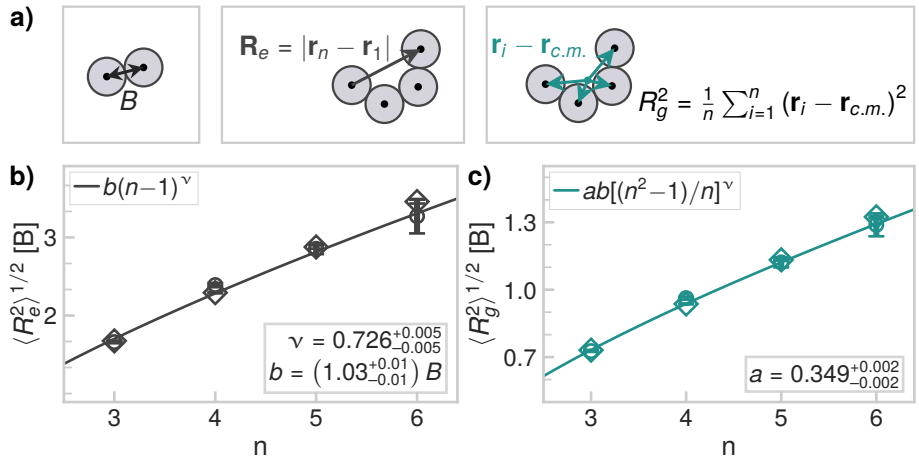

Figure 6.4: **RMS end-to-end distance and radius of gyration of flexible colloidal chains. a)** Left: the bond length B. Center: the end-to-end distance R_e. Right: definition of the radius of gyration R_g. **b)** Average R_e and fit of Equation 6.12 (fit values shown). **c)** Average R_g and fit of Equation 6.13 (fit values shown).

different measures for the conformations found in our experimental and simulated data, which we will discuss shortly. We compare these to predictions from polymer theory by simultaneously fitting Equations 6.12–6.15 to the corresponding values. We used a, b, ν, K, γ and C_g as fit parameters and report the maximum likelihood estimates (MLE), the error is given by the 16$^{\text{th}}$ and 84$^{\text{th}}$ percentiles of the posterior probability distributions (see Section 6.2.4 for details).

To compare our data to predictions based on polymer theory, we calculated the end-to-end distance R_e, where

$$R_e = |\boldsymbol{r}_n - \boldsymbol{r}_1|\,, \tag{6.10}$$

here $\boldsymbol{r}_i$ is the position of the i-th sphere. Additionally, we determined the radius of gyration R_g as follows,

$$R_g = \left[\frac{1}{n^2}\sum_{i=1}^{n}|\boldsymbol{r}_i - \boldsymbol{r}_{c.m.}|^2\right]^{1/2}, \tag{6.11}$$

with $\boldsymbol{r}_{c.m.}$ the center of mass (c.m.) of the cluster. Both R_e and R_g were normalized by the average interparticle distance B of each measurement and are schematically shown in Figure 6.4a. For long polymers, the root mean square (RMS) value of R_e can be described by a power law,[295]

$$\langle R_e^2 \rangle^{1/2} = b(n-1)^\nu, \tag{6.12}$$

where b is the Kuhn length (we expect $b \approx B$) and the Flory exponent $\nu = 3/(d+2) = 3/4$ for a self-avoiding walk in $d = 2$ dimensions.[296] Analogously, the RMS of R_g scales as[295]

$$\langle R_g^2 \rangle^{1/2} = ab[(n^2-1)/n]^{\nu}, \tag{6.13}$$

where the scaling constant $a \approx 1/\sqrt{6} \approx 0.41$.[297] We first test whether the behavior of our colloidal chains is comparable to long polymers in terms of RMS end-to-end distance and radius of gyration, as was shown for chains of flexibly linked oil droplets.[194]

Indeed, we find that the scaling of the RMS end-to-end distance and the RMS radius of gyration of these colloidal chains agree well with the predictions from polymer theory, as shown in Figure 6.4b (RMS end-to-end distance) and Figure 6.4c (RMS radius of gyration). For the Flory exponent we find $\nu = 0.726 \pm 0.005$, which is close to the exact value of $3/4$ for self-avoiding polymers in 2D and in agreement with the value found for flexibly linked chains of droplets ($\nu = 0.72 \pm 0.03$).[194] The Flory exponent is slightly lower than the expected value of $3/4$, this might be explained by the fact that we study a quasi-2D system, in which the particles have some freedom to move in the out-of-plane direction (for three dimensions $\nu \approx 0.6$[297]). In the simulations, we find an average center height of $(1.03^{+0.05}_{-0.02})R$ above the substrate (over a random subset of 1 % of the data, 7×10^5 positions). Although these excursions are small, they may lead to the slightly lower value of ν. On top of that, the slightly lower ν may be caused by the small number of beads per chain.

Next, we find that the Kuhn length $b = (1.03 \pm 0.01)B$ is in agreement with the hypothesis that it should be equal to the average bond length. In the experiments, the bond length is approximately twice the particle radius, plus the thickness of the bilayer ($\approx 4\,\mathrm{nm}$) and the length of the DNA linkers ($\approx 30\,\mathrm{nm}$). This leads to an estimated experimental bond length of $B \approx 1.03(2R)$. In the simulations, because of the harmonic potential that keeps the particles bonded, we find an average bond length of $B \approx (1.01 \pm 0.01)2R$ (over a random subset of 1 % of the data, 6×10^7 bonds). The fact that the Kuhn length is slightly greater than the bond length B may be explained by the greater-than-zero effective bending stiffness we have found in Figure 6.3c. As shown in Figure 6.4b, we find a shape factor $a = 0.349 \pm 0.002$, which is close to the expected value of $a \approx 0.41$[297] and the value found for flexibly linked chains of droplets ($a = 0.30 \pm 0.02$).[194]

So far we have found that the RMS end-to-end distance and radius of gyration of our colloidal chains show the same behavior as long polymers. When we look in greater detail into the free energy as function of end-to-end distances in Figure 6.5a, we see that our simulated data agrees very well with the permutation data, as well as the experimental data. Slightly larger deviations can be seen in the experimental data for n=5 and 6, this is due to the fact that because the number of configurations is very large for longer chains, increasingly larger amounts of data are needed to probe the equilibrium distribution (see Table 6.1 for a comparison between the amount of simulated and experimental data).

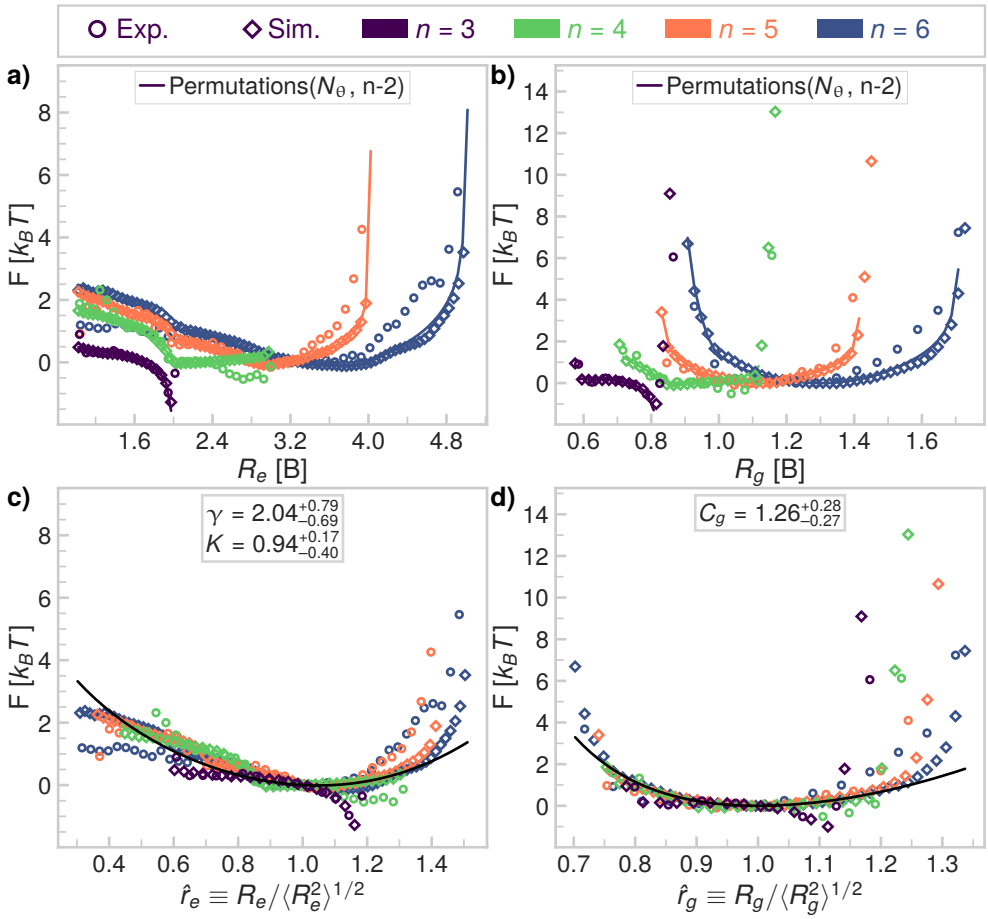

Figure 6.5: **Distributions of end-to-end distances and radii of gyration of flexible colloidal chains.** Markers for the ∘ experimental and ⋄ simulated data, together with the color coding legend for the different chain lengths n, as used in all are shown on top. **a-b)** Comparison between the free energy calculated for experimental, simulated and the $P(N_\theta, n-2)$ permutation data, as function of R_e (panel a) and R_g (panel b). **c)** Free energy in terms of $\hat{r}_e$ and fit of Equation 6.14 (fit values shown). **d)** Free energy in terms of $\hat{r}_g$ and fit of Equation 6.15 (fit values shown).

Based on polymer theory, the free energy of the reduced end-to-end distance $\hat{r}_e \equiv R_e/\langle R_e^2\rangle^{1/2}$ should collapse onto a master curve. For long, self-avoiding polymers, the free energy $F_e(\hat{r}_e)$ is expected to be equal to[298,299]

$$\frac{F_e(\hat{r}_e)}{k_BT} = (K\hat{r}_e)^\delta - (t+2)\ln\hat{r}_e - K^\delta \tag{6.14}$$

with $\delta = 1/(1-\nu)$, $t = (\gamma-1)/\nu$, K a positive constant and γ a positive exponent. This is indeed what we observe in Figure 6.5c. Furthermore, we see the agreement between model and simulated data is better for longer chains of n=5,6 compared to the shorter chains of n=3,4, where finite size effects play a larger role.

Finally, the free energy as function of the radius of gyration in Figure 6.5b is also very well described by the permutation data. It can be collapsed onto a master curve as function of the reduced radius of gyration $\hat{r}_g \equiv R_g/\langle R_g^2\rangle^{1/2}$ as given by[300]

$$\frac{F_g(\hat{r}_g)}{k_BT} = 2C_g\left[\frac{1}{\alpha}(\hat{r}_g)^{-d\alpha} + \frac{d}{\delta}(\hat{r}_g)^\delta + 1 - d\right], \tag{6.15}$$

with $\alpha = 1/(d\nu-1)$ and C_g a positive normalization constant. The resulting free energy is shown in Figure 6.5d. In terms of the reduced radius of gyration, deviations from the model are small even for n=4, while only the shortest chains of n=3 spheres show some deviations because of their finite size.

In summary, in this section we have characterized the conformations of flexibly linked colloidal chains of n=3 to 6 spheres. We find that while the chains are completely freely-jointed, some configurations are forbidden because they would result in interpenetrating particles. This affects the measured end-to-end distance and radius of gyration, especially for the shorter chains of n=3 and 4. Despite these finite size effects, we conclude that the conformations of all chains can be well described by polymer theory based on self-avoiding random walks. Based on the generality of the model and the agreement between model and data, we expect this to be true in general for other micron-sized objects in which self-avoidance plays a significant role.

6.3.2 Shape effects in the diffusion of flexible trimer and tetramer chains

Having characterized the equilibrium conformations of flexibly linked colloidal chains, we now analyze their shape-dependent short-time diffusive properties. Recently, we have studied the effect of flexibility on the diffusivity of the shortest chain, a freely-jointed trimer.[244] Similar to rigid particles, we found that shape affects the diffusive motion of the colloid at short timescales and that displacements are larger in directions that correspond to smaller hydrodynamic drag. Furthermore, we uncovered a Brownian quasiscallop mode, where diffusive motion is coupled to Brownian shape changes. At longer timescales, in addition to the rotational diffusion time, an analogous conformational diffusion time governs the relaxation of the diffusive motion, unique to flexible assemblies.[244]

The choice of coordinate system affects the magnitude of the diffusion tensor. For all rigid objects, there exist a tracking point relative to which the diffusion elements are independent of the lag time considered, called the center of hydrodynamic stress. Although such a point does not exist in general for flexible objects,[301] an analogous tracking point can be found where the magnitude of the diffusion tensor elements is minimal and therefore, close to the time-independent values at long lag times, called the center of diffusivity (c.d.).[269] We compare the results of two choices of tracking points, namely, the center of mass (c.m.) of the cluster which is another common choice, and the center of diffusivity (c.d.).[105,269]

The calculation of the c.d. is described in Section 6.2.5. We find that the c.d. is very close to the c.m. for all chain lengths, but a slightly larger weight is given to the outer particles compared to the particles in the center of the chain, as shown in Figure 6.7. The directions of the x- and y-axis of the body-centered coordinate system depends on the choice of reference point as given by Equation 6.4. For the trimer and tetramer chains, using the c.d. as tracking point, the body centered coordinate systems are shown in Figure 6.6a and Figure 6.1b/c, respectively. The rotational diffusivity is calculated from the angular displacements of the x-axis, or equivalently, rotations around an out-of-plane z axis perpendicular to x and y, as indicated in Figure 6.1b and Figure 6.6a. All diffusion tensor elements are calculated from Equation 6.1, the method is explained in detail in Section 6.2.5. The magnitude of the diffusion tensor elements relative to the c.m. compared to their magnitude relative to the c.d. is given in Figure 6.8 for a trimer. We find that for a trimer, differences in diffusivities relative to the c.m. and c.d. are only measurable for the rotational-translational coupling term and the Brownian quasiscallop mode, because the c.m. is very close to the c.d, as is shown in Figure 6.6a and in Figure 6.7.

The diffusivity of flexible trimers: simulations compared to experiments

We have analyzed the diffusivity of flexibly-linked trimers with respect to the c.d. and we now compare the experimental measurements to our simulations. As shown in Figure 6.6c, for the shape-dependent short-time rotational diffusivity, there is a quantitative agreement between the experiments and simulations for most opening angles. Next, we consider the flexibility, which is defined as half the slope of the mean squared angular displacements of the opening angle θ and defines how fast the chain changes its shape, defined analogously to Equation 6.1 for the tetramer chains and given for the trimers in our previous work.[244] As shown in Figure 6.6d, we measure a lower flexibility in the experiments compared to the simulations. This is caused by inter-particle friction stemming from the DNA linker patch embedded in the lipid membrane. Namely, it was found that increasing the DNA linker concentration leads to a decrease in the flexibility.[85]

Finally, we note that the experimental translational diffusivity is higher than the translational diffusivity obtained from the simulated data, as can be seen in Figure 6.6b. As a consequence, the experimentally determined translation-rotation coupling in Figure 6.6e, as well as the Brownian quasiscallop mode in Figure 6.6f are

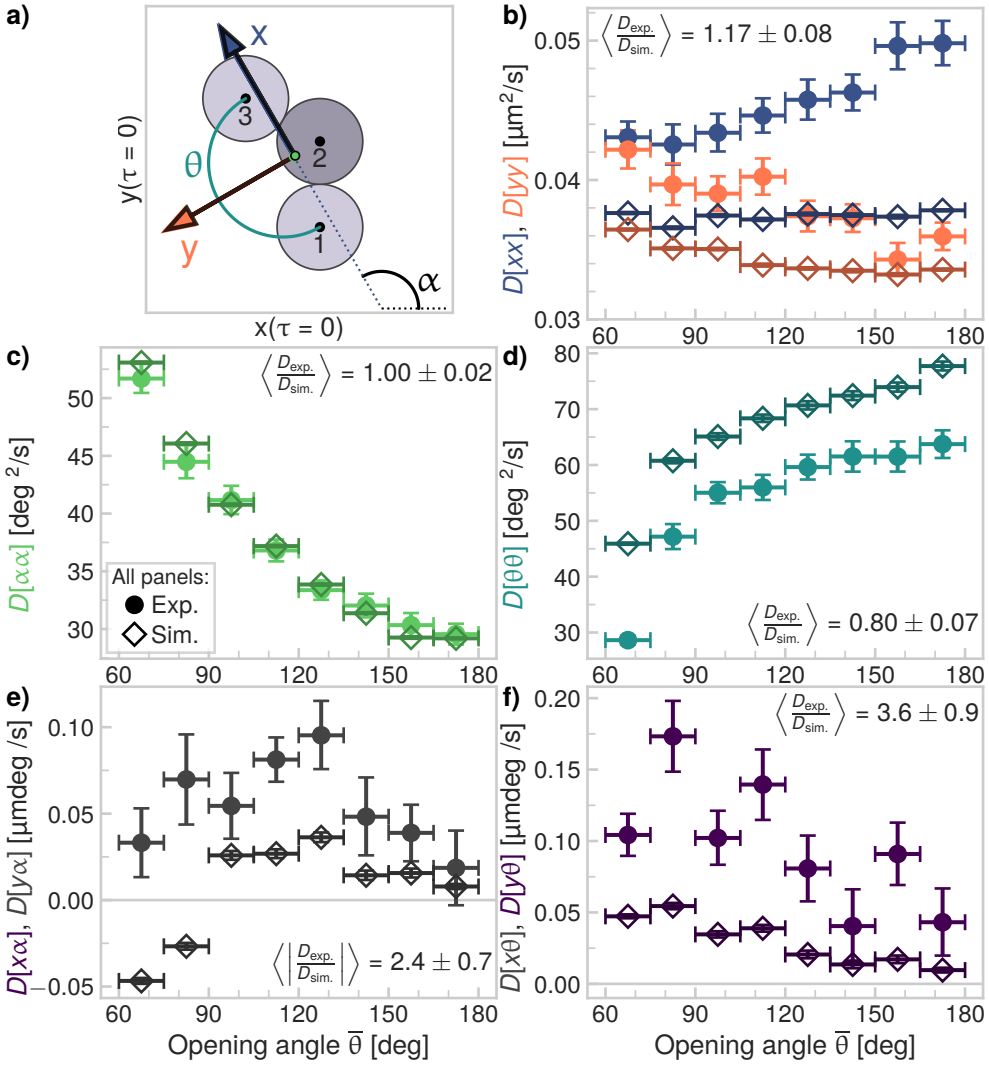

Figure 6.6: **Diffusivity of flexible trimers: experimental and simulated values.** Comparison between • experimental data and ⋄ simulated data (both $0.1 \leq \tau \leq 0.25$ s). **a)** Schematic depiction of the coordinate system of a trimer, as given by Equation 6.4. The colored arrows are calculated with respect to the c.d., while the black arrows are relative to the c.m. The difference between the two tracking points is very small, as shown in Figure 6.7. **b)** The experimental translational diffusivities are larger than the simulated ones, most likely caused by the difference in slip conditions in the experiments and simulations. **c)** The experimental rotational diffusivity is very close to the simulated values. **d)** The experimental flexibility is lower than the simulated values, because of friction stemming from the DNA linker patch. **e)** Translation-rotation coupling term $D[x\alpha]$. **f)** Translation-flexibility coupling term: the Brownian quasiscallop mode $D[y\theta]$.[244]

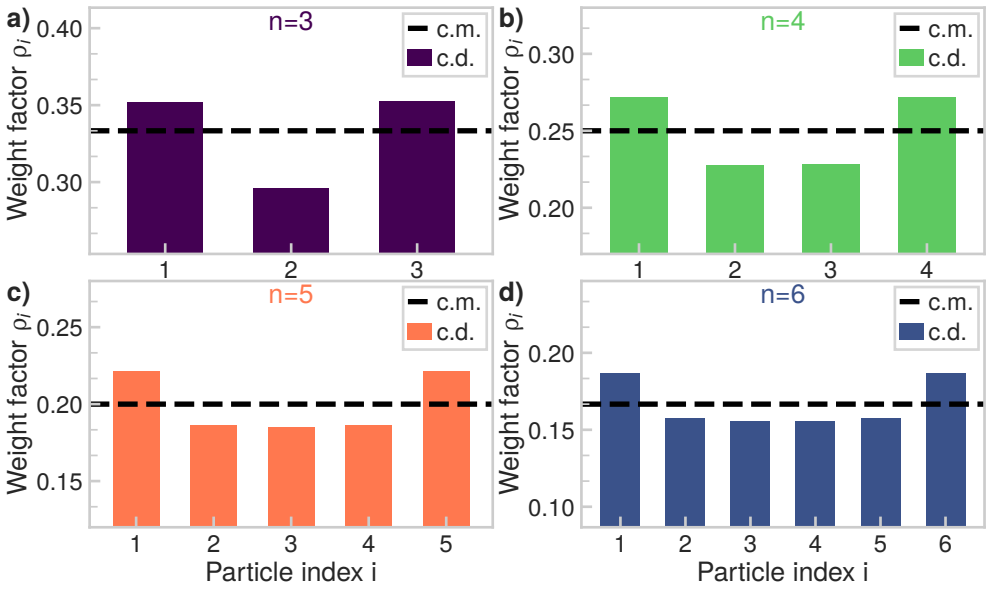

Figure 6.7: **Center of diffusion (c.d.) versus center of mass (c.m.): weight factors.** Weight factors ρ for the c.m. and the c.d., for **a)** trimer (n=3) **b)** tetramer (n=4) **c)** pentamer (n=5) **d)** hexamer (n=6) chains. For the c.d., more weight is accorded to the outer particles compared to the inner particles of the chain. However, differences between the c.m. and the c.d. are small for all chain lengths.

also higher than the values determined from the simulations. This is likely caused by the fact that we model the substrate as a no-slip surface in the simulations, whereas in the experiment the substrate is coated with a hydrogel to prevent particles from sticking, which has a nonzero slip length. We think that this nonzero slip length in the experiments leads to higher translational diffusivities in the experiments, because the particles move further away from the glass and so there is less friction caused by the effectively more viscous water layer close to the no-slip glass substrate.

Effect of tracking point, bin width and lag time on the diffusivity of flexible trimers

The choice of coordinate system affects the magnitude of the diffusion tensor. For all rigid objects, there exist a tracking point relative to which the diffusion elements are independent of the lag time considered, called the center of hydrodynamic stress. Although such a point does not exist in general for flexible objects,[301] an analogous tracking point can be found where the magnitude of the diffusion tensor elements is minimal and therefore, close to the time-independent values at long lag times, called the center of diffusivity (c.d.).[269] We compare the results of two choices of tracking points, namely, the center of mass (c.m.) of the cluster which is another common choice, and the center of diffusivity (c.d.).[105,269]

First, as shown in Figure 6.7, the c.d. is very close to the c.m. for all chain lengths. A slightly larger weight is given to the outer particles for the c.d. compared to the c.m., but this has only a very small effect on the location of the c.d. Second, we compare the magnitude of the diffusion tensor of a flexible trimer relative to the c.m. as in our previous work[244] and relative to the c.d. (this work). As shown in Figure 6.8, the translational (Figure 6.8b), rotational (Figure 6.8c) and flexibility (Figure 6.8d) terms of the diffusion tensor are only slightly affected by changing the tracking point from the c.m. to the c.d. This is easily explained by the fact that the position of the c.d. only changes by approximately 6 % for the smallest opening angle compared to the c.m., as shown in Figure 6.8a. However, the coupling terms are lower with respect to the c.d. as shown in Figure 6.8e for the translation-rotation coupling term and in Figure 6.8f for the Brownian quasiscallop mode. The fact that these coupling terms are lower is expected, because the magnitude of the diffusion tensor is expected to be the lowest relative to the c.d., as it is closest to the long-time diffusion tensor, for which short-time correlations or memory effects are expected to vanish.

The simulations allow us to probe the diffusivity at arbitrarily high frame rates and thus arbitrarily short lag times τ, which is the time delay between the pairs of frames considered in the calculation of the mean squared displacements. There is a marked effect of lag time on the flexibility, as shown in Figure 6.9d. For the simulated data, we show the results for a lag time of 0.05 s (diamonds) and 0.1 to 0.25 s (squares, same lag time as experimental data). The lag times of the experimental data range from 0.1 to 0.25 s, as set by the frame rate of the camera. The simulated data with longer lag times are close to the experimental data. However, when we analyze the simulated data using a shorter lag time, we find a large increase in the flexibility. This difference can easily be explained by considering the mean squared angular displacement of the opening angle in Figure 6.9a. Especially for the larger opening angles, we see that the mean squared displacements show a plateau at longer lag times, leading to a smaller apparent flexibility when the data is fitted using a linear model. The effect of lag time is also present in the Brownian quasiscallop mode in Figure 6.9f. For terms not directly related to flexibility, such as translational diffusivity in Figure 6.9b, rotational diffusivity in Figure 6.9c and translation-rotation coupling in Figure 6.9e, we see there is no appreciable effect of different lag times.

This plateauing for flexibility-related diffusion terms is caused by the calculation method of the shape-dependent diffusivity. That is, we consider only those pairs of frames where the shape of the particle stays within the limits of the particular opening angle bin of the first frame. Therefore, if the flexibility is high, a large percentage of frames will exceed the initial bin and these will not be considered in the analysis. The frames where the bin is not exceeded, as a result, are those in which the flexibility is lower, which leads to the apparent decrease in flexibility at longer lag times.

To solve this, larger bin widths can be used at the expense of a lower resolution in opening angle. We tested this in Figure 6.9d and found that indeed, the values for the flexibility were higher, while the other diffusion tensor elements were not affected (see Figure 6.9, crosses). In fact, by using a larger bin width, we measure

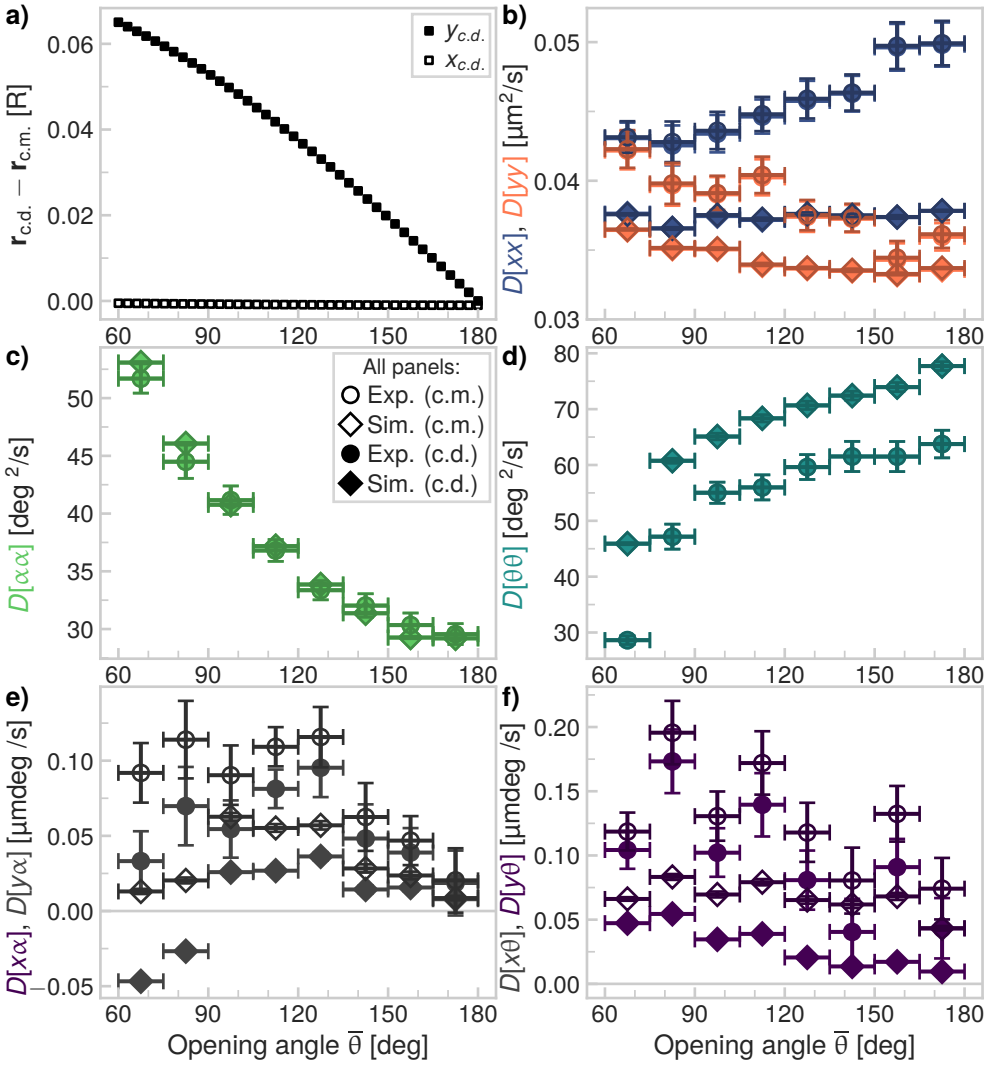

Figure 6.8: **Center of diffusion (c.d.) versus center of mass (c.m.) as tracking point.** For all panels, open points correspond to the c.m. as tracking point while filled points refer to the c.d. as tracking point. ∘ experimental data, ⋄ simulated data (both $0.1 \leq \tau \leq 0.25$ s). **a)** The c.d. of flexible trimers is very close to the c.m.: there is only a small deviation of approximately 6 % for the smallest opening angles. The difference $\boldsymbol{r}_{c.d.} - \boldsymbol{r}_{c.m.}$ on the y-axis is given in terms of R. **b)** The translational diffusivity changes only slightly with respect to a different tracking point. **c)** The rotational diffusivity does not change as function of tracking point. **d)** Also for the flexibility term, there is no influence of tracking point. **e)** The effect of tracking point for rotation-translation coupling is more pronounced: values are lower when the c.d. is used as tracking point. **f)** Also for the Brownian quasiscallop mode, the values are lower when using the c.d. as tracking point instead of the c.m.

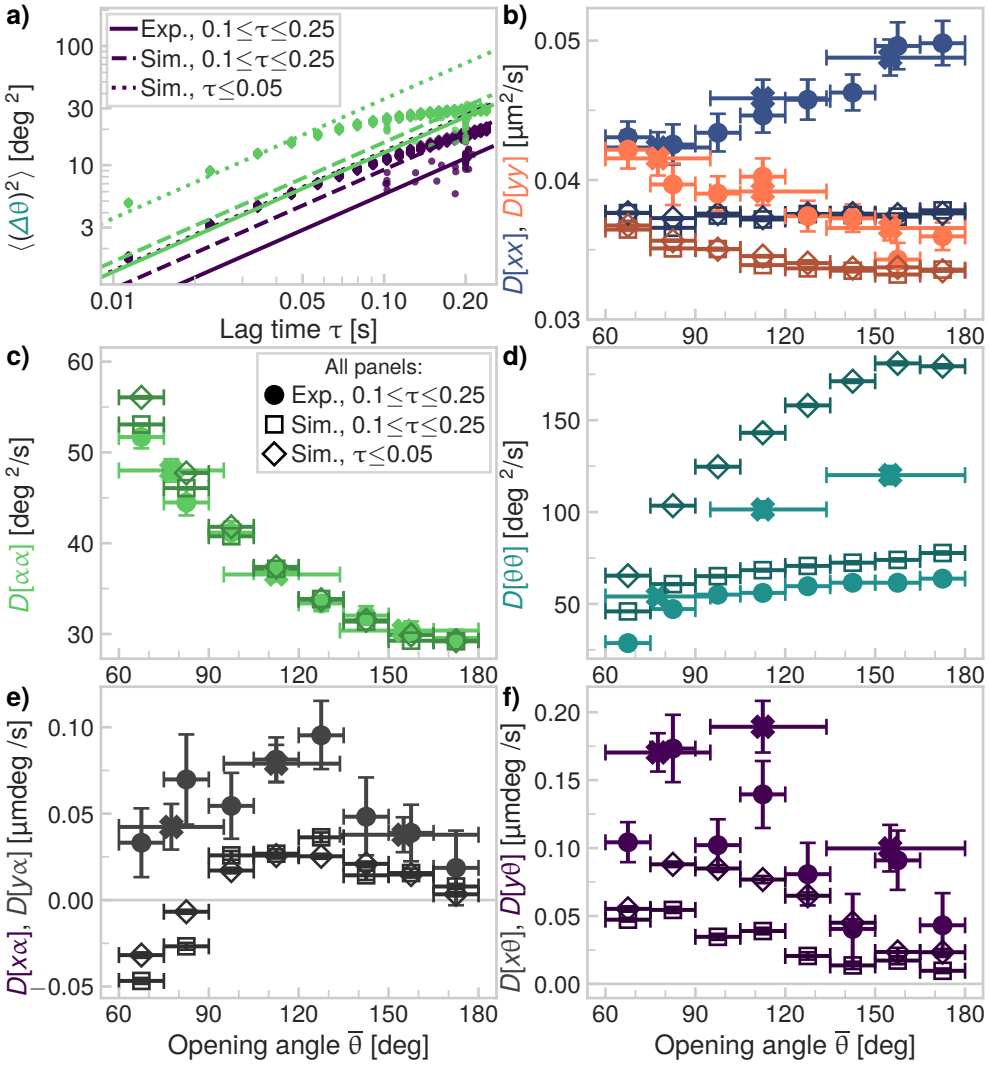

Figure 6.9: **Trimer: effect of varying the bin size / lag time** Comparison between • experimental data, × experimental data with a larger bin width (both $0.1 \leq \tau \leq 0.25\,\mathrm{s}$) and simulated data: ⋄ $\tau \leq 0.05\,\mathrm{s}$, □ $0.1 \leq \tau \leq 0.25\,\mathrm{s}$. **a)** Mean-squared angular displacement of the opening angle reveals caging effects at longer lagtimes, which are more pronounced for higher flexibilities, an effect inherent to the analysis method. **b)** The translational diffusivities are less sensitive to the choice of lagtimes. The experimental translational diffusivities are larger than the simulated ones. **c)** The rotational diffusivities are largely unaffected by the different choices for lagtimes (except for small opening angles), the experimental data agrees with the simulated data. **d)** The flexibility is highly sensitive for the choice of lagtimes. **e)** Translation-rotation coupling terms. **f)** Translation-flexibility coupling terms, including the Brownian quasiscallop mode $D[y\theta]$,[244] which is sensitive to the choice of lagtimes.

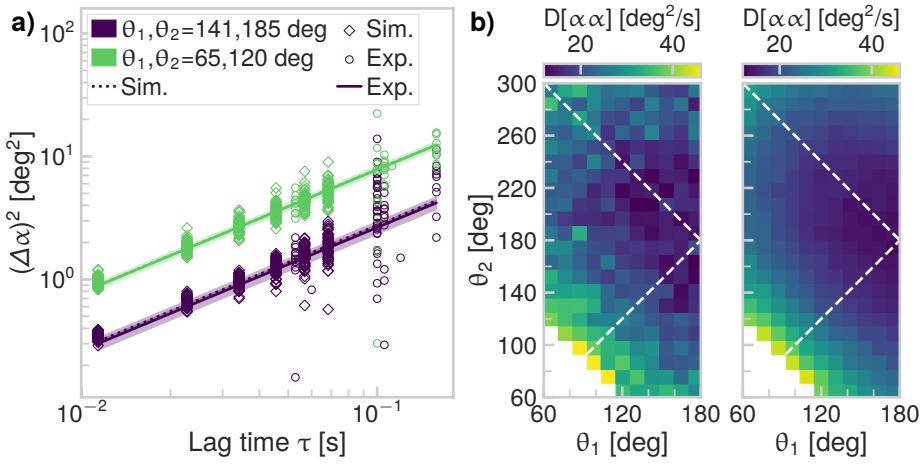

Figure 6.10: **Rotational diffusion of flexible tetramer chains. a)** The mean squared angular displacement for a compact configuration (green) is larger than that of an extended configuration (purple). The elements of the diffusion tensor are obtained by fitting the slope of mean squared displacements. **b)** The rotational diffusivity is highest for compact shapes. The left plot shows experimental data and the right plot shows simulated data. For fitting, we use a maximum lag time $\tau = 0.17\,\mathrm{s}$. The dashed lines indicate the two symmetry axes of the opening angles, $\theta_2 = \theta_1$ and $\theta_2 = 360\,\mathrm{deg} - \theta_1$.

the "true" short-time flexibility: the ratio between the experimental flexibility for the smaller bins (circles in Figure 6.9d) and the simulated flexibility for the experimental lag times (squares in Figure 6.9d) is equal to 0.78 ± 0.07. By using the larger bins, the ratio between the experimental flexibility and the simulated flexibility at short lag times (diamonds in Figure 6.9d) is also equal to 0.77 ± 0.07.

In conclusion, the diffusivity of the c.d. is very close to that relative to the c.m. Interestingly, the interplay of lag time and bin width has a critical effect on the measured short-time diffusion tensor elements related to shape changes and should be carefully considered in the analysis of experimental data.

The diffusivity of flexible colloidal tetramer chains

Having established that the simulations can faithfully describe the short-time shape dependent diffusivity of flexible trimers, in addition to the equilibrium conformations of flexible chains, we now analyze the diffusivity of flexible tetramer chains. In Figure 6.10a, we show that the rotational diffusivity for compacter shapes is higher than that of more extended shapes for two examples, $\theta_1, \theta_2 = 65, 120\,\mathrm{deg}$ (compact) and $\theta_1, \theta_2 = 141, 185\,\mathrm{deg}$ (extended). Furthermore, we conclude that the simulated data agrees with the experimental data, within experimental error. This can also be seen for the rotational diffusivity as function of opening angles θ_1, θ_2 in Figure 6.10b.

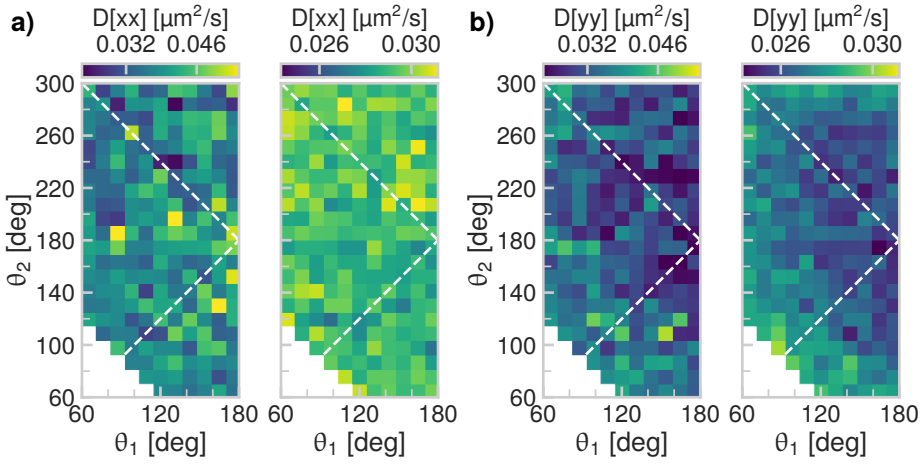

Figure 6.11: **Translational diffusion of flexible tetramer chains.** In both panels, the left plot shows experimental data and the right plot shows simulated data. For fitting, we use a maximum lag time $\tau = 0.17\,\mathrm{s}$. The dashed lines indicate the two symmetry axes of the opening angles, $\theta_2 = \theta_1$ and $\theta_2 = 360\,\mathrm{deg} - \theta_1$. **a)** The translational diffusivity in the x-direction as function of the opening angles θ_1, θ_2, as depicted in Figure 6.1b and c. **b)** Translational diffusivity in the y-direction, which is lower for chains with a stretched angle (θ_1, θ_2 close to 180 deg). For both translational terms, we use different color scales for the experimental and simulated data, because the experimental diffusivities are higher than the simulated ones.

The symmetry lines of the opening angles $\theta_2 = \theta_1$ and $\theta_2 = 360\,\mathrm{deg} - \theta_1$ are indicated as well. The configurations are symmetric around these lines except for the fact that we break this symmetry by choosing which angle to label as θ_1 and which as θ_2, because this has consequences for the orientation of the body centered coordinate system, as shown in Figure 6.1c and defined in Equation 6.4. However, for the rotational diffusivity we only consider angular rotations of the x-axis and therefore the rotational diffusivity is indeed symmetric with respect to the symmetry lines of the opening angles.

For the translational diffusivity in the x-direction (Figure 6.11a) and y-direction (Figure 6.11b) we note that the experimental diffusivity is again slightly larger than the simulated one, similar to the trimers in Figure 6.6b. Again, this is because of the no-slip condition in the simulations versus the hydrogel surface used in experiments to prevent particles from sticking, which has a nonzero slip length. Because the translational diffusivity does not depend on whether the x-axis points to one end of the chain or the other, or equivalently, whether the y-axis points towards one side or the other, we expect that translational diffusivity is symmetric with respect to the symmetry lines of the opening angles. This is indeed true: we observe little shape dependence for translational diffusivity in the x-direction in Figure 6.11a, variations

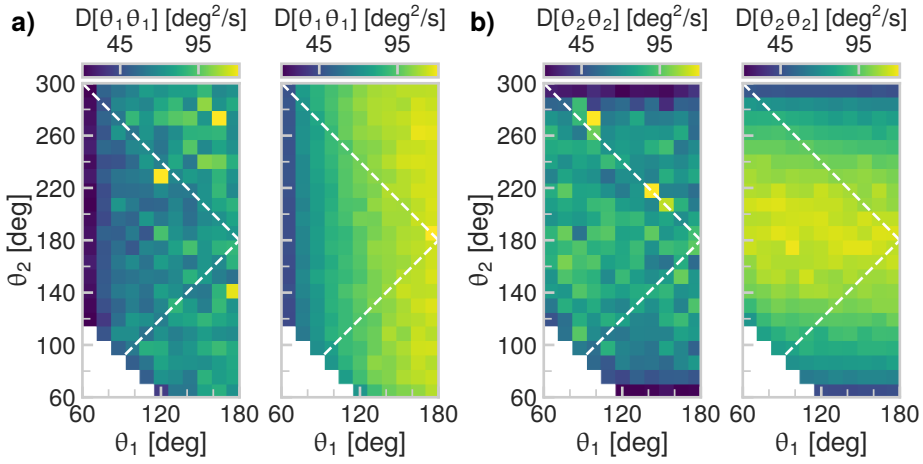

Figure 6.12: **Flexibility of tetramer chains.** In both panels, the left plot shows experimental data and the right plot shows simulated data. For fitting, we use a maximum lag time $\tau = 0.17\,\mathrm{s}$. The dashed lines indicate the two symmetry axes of the opening angles, $\theta_2 = \theta_1$ and $\theta_2 = 360\,\mathrm{deg} - \theta_1$. **a)** The flexibility in the opening angle θ_1 shows a maximum for $\theta_1 = 180\,\mathrm{deg}$. **b)** The flexibility in the opening angle θ_2 also has its maximum value for $\theta_2 = 180\,\mathrm{deg}$.

are likely due to experimental noise. On the contrary, the diffusivity in the y-direction in Figure 6.11b is lower for more extended shapes, which correspond to larger surface areas and therefore, a larger hydrodynamic drag. We note that it is also symmetric with respect to the opening angle symmetry lines.

Interestingly, for the diffusivity of the opening angles in Figure 6.12a (θ_1) and Figure 6.12b (θ_2), we note that the flexibility is highest for opening angles θ_1, θ_2 close to 180 deg (i.e. more extended chains). This is in agreement with the trends we have observed for the flexible trimers in Figure 6.6d and our previous work[244] and suggests that hydrodynamic interactions between the particles slow down shape changes for small inter-particle separation distances. Furthermore, we note that the flexibility is not symmetric around the opening angle symmetry lines, because we have broken the symmetry in this case, by labeling one angle as θ_1 and the other one as θ_2.

The experimental flexibility data in Figure 6.6d shows the same trends as the simulated data but is lower in magnitude. Because the flexibility depends on the concentration of DNA linkers,[85] which cause additional friction in the bond area, this could also explain the lower flexibility found in the experimental data, absent in the simulations. Similarly to what we have found for the trimers in Figure 6.6d, we find that the experimental flexibility in θ_1 is $(71 \pm 12)\,\%$ of the simulated one, for θ_2 this is $(75 \pm 14)\,\%$. Therefore, we conclude that the lower magnitude is indeed caused by friction stemming from the DNA linker patch.

The off-diagonal elements of the diffusion tensor describe possible coupling terms.

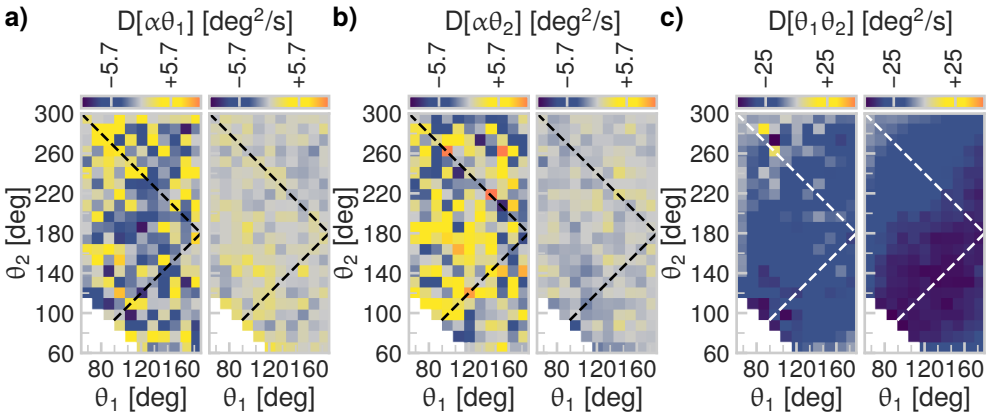

Figure 6.13: **Diffusion of flexible tetramer chains: coupling terms.** In all panels, the left plot shows experimental data and the right plot shows simulated data. For fitting, we use a maximum lag time $\tau = 0.17\,\mathrm{s}$. The dashed lines indicate the two symmetry axes of the opening angles, $\theta_2 = \theta_1$ and $\theta_2 = 360\,\mathrm{deg} - \theta_1$. **a)** The rotation-flexibility coupling $\mathrm{D}[\alpha\theta_1]$ is close to zero. **b)** The rotation-flexibility coupling $\mathrm{D}[\alpha\theta_2]$ is also close to zero. **c)** There is a strong negative coupling in flexibilities of the two opening angles θ_1, θ_2.

We have calculated those terms and find that there is no significant coupling between rotational diffusivity and flexibility, as shown in Figure 6.13a for the coupling between α and θ_1 and in Figure 6.13b for $\mathrm{D}[\alpha\theta_2]$. This is the same result we have found for flexible trimers[244] and we hypothesize this can be generalized to larger chain lengths as well.

However, there is a strong negative coupling between diffusivities in the two opening angles θ_1, θ_2, as shown in Figure 6.13c, which is symmetric with respect to the symmetry lines of the opening angles. In fact, the negative coupling is strongest around the symmetry line $\theta_1 = \theta_2$ and lowest for zig-zag like structures near $\theta_1 = 60\,\mathrm{deg}$ and $\theta_2 = 300\,\mathrm{deg}$. By comparing Figure 6.13c to the schematics of possible conformations in Figure 6.1c, the configurations where the negative couplings are highest, are those where the outer particles are both on the same side of the coordinate system, namely the positive y plane. There, the hydrodynamic interactions between the particles are largest and therefore also the negative coupling is largest.

Interestingly, we also find small, but nonzero coupling terms for translation-rotation coupling. By comparing the two translation-rotation coupling terms, we note that $y\alpha$ in Figure 6.14d is small compared to $x\alpha$ in Figure 6.14a, for both the experimental and simulated data. This means that displacements in the positive x-direction (see Figure 6.1c) will lead to counter-clockwise rotations of the chain, similarly to the $x\alpha$ coupling we found for the trimers,[244] as also shown here in Figure 6.6e.

Lastly, by comparing the translation-flexibility coupling terms for both opening

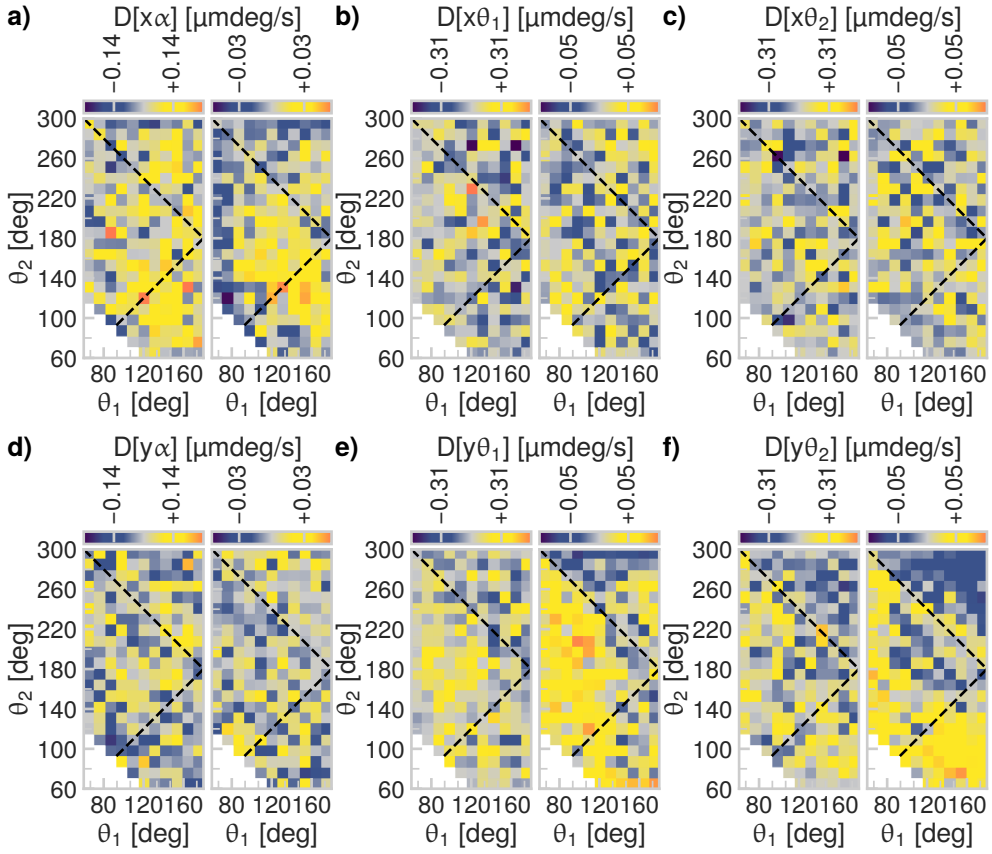

Figure 6.14: **Diffusion of flexible tetramer chains: translational coupling terms.** In all panels, the left plot shows experimental data and the right plot shows simulated data. The color scales of the experimental and simulated data are different, because the experimental translational diffusivity is higher than the simulated one. For fitting, we use a maximum lag time $\tau = 0.17\,\mathrm{s}$. The dashed lines indicate the two symmetry axes of the opening angles, $\theta_2 = \theta_1$ and $\theta_2 = 360\,\mathrm{deg} - \theta_1$. **a)** There is a small translation-rotation coupling D[xα]. **b)** The translation-flexibility coupling D[xθ_1] is close to zero. **c)** The translation-flexibility coupling D[xθ_2] is also close to zero. **d)** The translation-rotation coupling D[yα] is zero as well. **e)** There exists a nonzero translation-flexibility coupling D[yθ_1]. **f)** The translation-flexibility coupling D[yθ_2] is also nonzero.

angles in the x-direction, shown in Figure 6.14b for $x\theta_1$ and Figure 6.14c for $x\theta_2$, and in the y-direction, see Figure 6.14e for $y\theta_1$ and Figure 6.14f for $y\theta_2$, we observe that the coupling terms related to the y-direction are larger in magnitude than those in the x-direction. For the x-direction, there are no clear trends for either opening angle, in both the simulated and the experimental data, as shown in Figure 6.14b and c. On the contrary, for translation-flexibility coupling terms in the y-direction, we find couplings, analogously to the Brownian quasiscallop mode we have found for trimers,[244] also shown in Figure 6.6f.

By looking closely at the coupling between y and θ_1 diffusivity in Figure 6.14e, we observe that the coupling is positive for angles above the symmetry line $\theta_1 = \theta_2$ and below the symmetry line $\theta_1 = 360\,\text{deg} - \theta_2$. If we look at the configurations for these angles in Figure 6.1c, we observe that positive y-displacements lead to an opening of one end of the chain, namely the trimer segment with opening angle θ_1, similar to the Brownian quasiscallop mode for trimers. We see the same effect for configurations below the symmetry line $\theta_1 = \theta_2$ and in fact, the coupling is symmetric around this symmetry line. For configurations above the other symmetry line, $\theta_1 = 360\,\text{deg} - \theta_2$, there are strongly negative correlation terms, especially near $\theta_2 = 300\,\text{deg}$. By again studying the configurations for these angles in Figure 6.1c, we note that this is indeed what would be expected to happen for the trimer segment with opening angle θ_1, based on our earlier findings of the Brownian quasiscallop mode in trimers. Apart from the expected negative correlations we expect from the Brownian quasiscallop mode of a trimer, there are also positive values in this region. However, we cannot compare them directly, because the coordinate system, and therefore the direction of the y-axis, is different in the case of a tetramer chain. Specifically, it is not centered on the trimer segment. Therefore, the coupling we have observed is similar to, but more complex than the Brownian quasiscallop mode in trimers.

Analogously, we observe the same effects for the coupling between diffusivity in the y-direction and the other opening angle θ_2, as shown in Figure 6.14f. Starting below the symmetry line $\theta_1 = \theta_2$, the coupling is positive, as expected. Above the other symmetry line $\theta_1 = 360\,\text{deg} - \theta_2$, we observe the opposite, negative coupling, which is in line with our previous results for the opening angle θ_1. Between the two symmetry lines, something more complicated happens, analogously to the area above the symmetry line $\theta_1 = 360\,\text{deg} - \theta_2$ for the D[yθ_1] coupling discussed previously. There, we observe a positive coupling for configurations close to $\theta_1 = 60\,\text{deg}$, as expected from the Brownian quasiscallop mode and the other coupling term D[yθ_1]. For the other configurations in the area between the symmetry lines, we observe both positive and negative coupling terms. Therefore, we conclude that there the behavior is also more complex than one would expect based on the assumption that the individual trimer segments show Brownian quasiscallop modes. This is likely due to the displacement of the coordinate system from the center of the trimer segment, as well as possible hydrodynamic couplings between shape changes, as we have observed in Figure 6.13c.

In summary, in this section we have shown that for both trimers and tetramers,

the flexibility determined from the experimental data is reduced to approximately 75 to 80 % of the flexibility determined from simulations, because of friction of the DNA linker patch, which is not modeled in the simulations. We have found marked flexibility-induced effects on the diffusivity of flexible tetramer chains, namely an increase in flexibility for the more elongated configurations and nonzero couplings between translational diffusivity and both rotational diffusivity and flexibility, as well as a strongly negative coupling between diffusivity of the two opening angles. We have established that the simulations can adequately model our experimental findings, especially for terms that do not relate to translational diffusivity. For the translational terms, the slip conditions on the surface play a crucial role and require further careful consideration in future works.

6.3.3 Shape-averaged diffusion of flexible chains

We have studied the short-time, shape dependent diffusivity of flexible trimer and tetramer chains. For the longer pentamer (n=5) and hexamer (n=6) chains, studying the diffusion tensor as function of shape is more challenging because of the greater number of opening angles and consequently, greater number of degrees of freedom. Therefore, we take an approach known as the rigid-body approximation [101,264,286,287] and study the shape-averaged short-time diffusivity.

In Figure 6.15a we show the translational diffusivity as function of chain length for experimental and simulated data, relative to the c.d. and the c.m. As we have argued before in Section 6.3.2, different choices of tracking points can lead to different magnitudes of the diffusion tensor elements. For flexible objects, the c.d. is the most appropriate tracking point to use, because it gives the smallest values of the diffusion tensor elements and therefore the obtained values are closer to the long time diffusivities. [269] For the flexible colloidal chains, the c.d. turns out to be very close to the c.m. for all chain lengths, but a slightly larger weight is given to the outer particles compared to the particles in the center of the chain. Because the c.m. is very close to the c.d. (see Figure 6.7 for a comparison), we conclude that for our flexibly linked chains, there is no appreciable difference between the two different choices of tracking point, both for the experimental and simulated data.

In Figure 6.15a, we see a clear scaling of diffusion coefficient D_T with chain length and hypothesize that this scaling can be described by polymer theory. In Kirkwood-Riseman theory, [286] the translational diffusion coefficient is expected to be proportional to $\propto \langle R_g^2 \rangle^{-\nu/2}$. Indeed, we find that for the experimental data, the fitted $\nu = 0.7 \pm 0.5$ is close to the expected value of 3/4. More clearly, for the simulated data, we find $\nu = 0.77 \pm 0.02$. Again, the average experimental translational diffusivity is higher than the simulated one, because of differences in the surface slip conditions, as explained in Section 6.3.2. Therefore, Kirkwood-Riseman theory can be used to describe the scaling of the translational diffusivity of the chains as function of their length.

Additionally, we have calculated the lower bound on the short-time diffusion coefficient $D_{c.d.}$, because its value should be close to the long-time diffusion coefficient

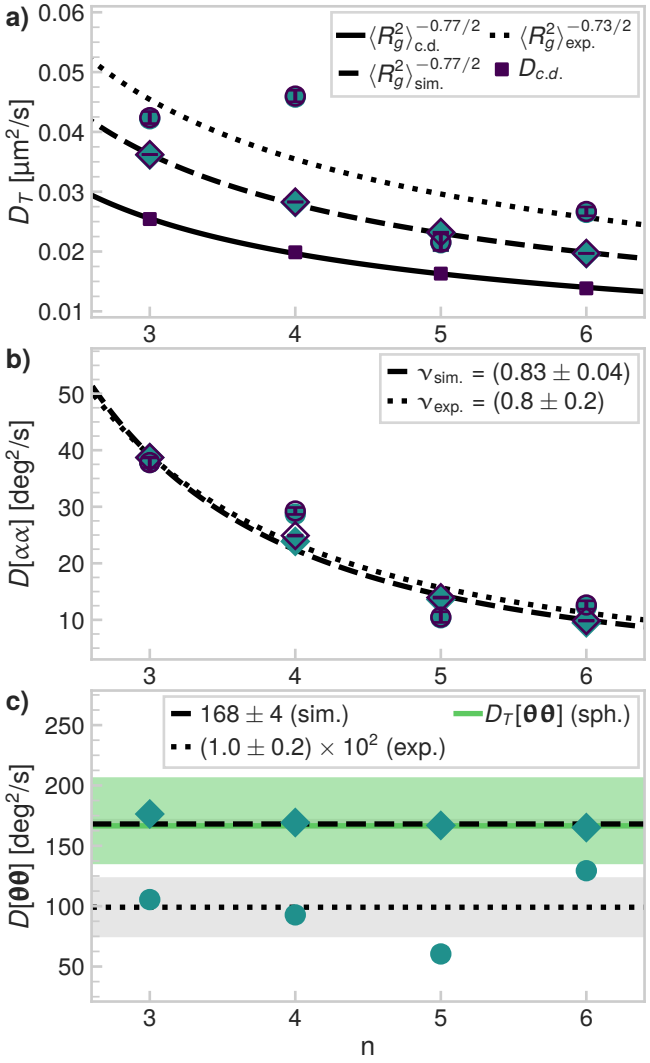

Figure 6.15: **Average diffusivity of flexible colloidal chains.** All panels: ∘ experimental data ($\tau \leq 0.25\,s$), ⋄ simulated data ($\tau \leq 0.05\,s$). **a)** In plane translational diffusion coefficient D_T as function of chain length. **b)** Rotational diffusion coefficient $D[\alpha\alpha]$ (around the axis normal to the substrate) as function of chain length. **c)** Flexibility coefficient $D[\boldsymbol{\theta\theta}]$ as function of chain length. The flexibility does not depend on chain length, the median values plus standard deviations are indicated for both the experimental and simulated data.

typically measured in scattering experiments.[269] We determined $D_{c.d.}$ from the matrix $\boldsymbol{A}_{ij}$ defined by Equation 2.16 of Cichocki et al.[269] using the RPB tensor[35] with lubrication corrections as the inter-particle mobility matrix $\boldsymbol{\mu}_{ij}$ (see also Section 6.2.5 for details). Indeed, we find that its value is always lower than the simulated or experimental values, which indicates that memory effects, or in other words, time correlations, play a large role in the translational diffusivity of our clusters. We find the same scaling as function of chain length as for the experimental and simulated data, namely, $\nu = 0.77 \pm 0.02$, as predicted by Kirkwood-Riseman theory.

Next, having characterized the translational diffusivity of the flexible chains, we now consider their rotational diffusivity $D[\alpha\alpha]$. While there is no unique choice for which axis to use to quantify the rotational diffusivity of a shape-changing object, we use the definition in Equation 6.4 for consistency. As shown in Figure 6.15b, the simulated data agree with the experimental data and the differences between using the c.m. or the c.d. as tracking point are minimal. We use an approximate expression to describe the rotational diffusivity of our flexible chains in the rigid rod limit:[286]

$$D[\alpha\alpha] \propto \frac{\ln\left(2L/d\right)}{L^3}, \tag{6.16}$$

with L the length of the rod and d its diameter. Setting $d = b$ (the Kuhn length) and $L = b\left(1 + (n-1)^{\nu}\right)$, which is the average end-to-end distance plus the Kuhn length, we obtain a reasonable fit with ν close to the expected 3/4, as shown in Figure 6.15b. Specifically, we find $\nu = 0.8 \pm 0.2$ for the experimental data and $\nu = 0.83 \pm 0.04$ for the simulated data. Therefore, we conclude that while the shape dependent short time diffusivity of flexible colloidal chains shows clear flexibility effects as discussed in Section 6.3.2, the scaling of the shape-averaged translational and rotational diffusion coefficients can be described very well by the rigid body approximation.

In Section 6.3.2, we have found couplings between translational diffusivity and both rotational diffusivity and the flexibility of trimers and tetramers, for the shape-dependent diffusion tensor. We have calculated the shape-averaged translation-flexibility and translational-rotational coupling terms with respect to both the c.m. and the c.d., as shown in Figure 6.16. The shape-averaged translation-flexibility coupling modes in the y-direction are positive for a trimer, which corresponds to the Brownian quasiscallop mode[244] of the shape-dependent diffusion tensor, as shown in Figure 6.16a. For longer chain lengths, this coupling term is averaged out, most likely because of the negative correlation we have found between the flexibility of the two opening angles of the tetramer chain, which indicates that such coupling terms may be present for longer chain lengths as well. Because the coordinate system is not centered on the trimer segment, overall shape changes are taken into account. We find that overall, there is no average coupling between translational diffusivity in the y-direction and the overall flexibility $D[\boldsymbol{\theta}\boldsymbol{\theta}]$.

On the contrary, in Figure 6.16b, we see that there is a positive coupling between rotational diffusivity and translational diffusivity in the x-direction, which decreases

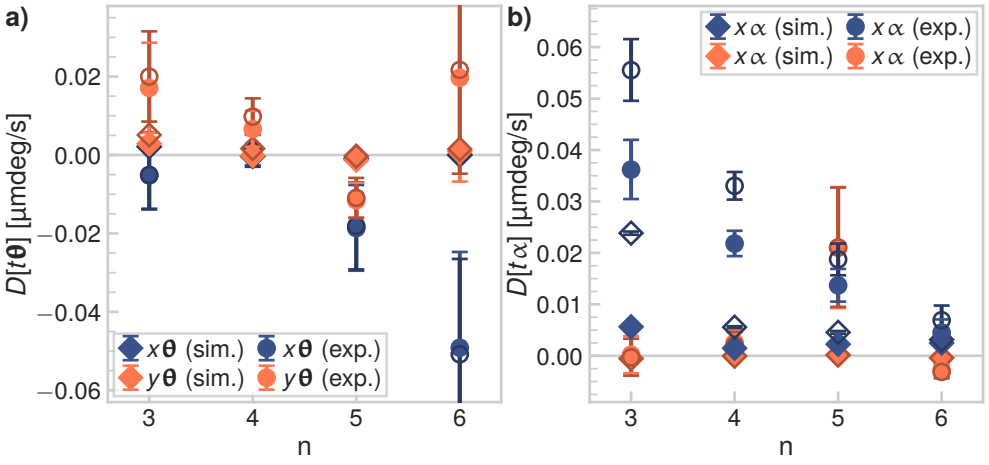

Figure 6.16: **Shape-averaged coupling terms as function of chain length.** In all panels, filled symbols are with respect to the c.d. and unfilled symbols are with respect to the c.m. **a)** The shape-averaged translation-flexibility coupling modes in the y-direction are positive for a trimer (Brownian quasiscallop mode) but average out for larger chain lengths. **b)** The shape-averaged translation-rotation coupling mode in the x-direction is positive for trimers and decreases as function of chain length.

as function of chain length. This is the same coupling we have found for the shape-dependent diffusion tensor of both trimers[244] and tetramers.

Finally, we consider the shape-averaged flexibility $D[\boldsymbol{\theta}\boldsymbol{\theta}]$ by calculating the slope of the mean squared angular displacements of the $n-2$ opening angles $\langle|\Delta\boldsymbol{\theta}|^2\rangle$ as function of lag time, as defined by Equations 6.2–6.3. First, we observe that the mean squared displacements of $\Delta\boldsymbol{\theta}$ increase linearly with lag time, similarly to the other diffusion tensor terms. Moreover, we find that the flexibility is independent of the length of the chain, as shown in Figure 6.15c.

As we have seen for the shape-dependent short-time flexibilities of the trimer and tetramer in Figure 6.6d and Figure 6.12 respectively, the average experimental flexibility is approximately 75 to 80 % of the average flexibility in the simulations. We hypothesize that the lower flexibility in the experiments is caused by inter-particle friction stemming from the DNA linkers. This is also supported by the observation that while the experimental flexibility shows large fluctuations, that are due to experimental differences in DNA concentration between particles and samples, the flexibility in the simulations shows a very narrow distribution. For the shape-averaged flexibility, we find that the experimental flexibility averaged over all chain lengths is (60 ± 15) % of the simulated one, where the spread is most likely caused by the spread in the DNA linker concentration.

For trimers of flexibly-linked emulsion droplets, it was proposed that for small displacements of the opening angle, the maximum value of the flexibility is expected

to be dominated by the translational friction coefficient of the particles.[194] However, in the droplet-based system, the flexibility was found to be unaffected by the DNA linker concentration.[194] Because of this difference, we test whether the same behavior applies to our flexibly linked chains of colloidal particles, in spite of the presumably different dynamics, caused by the friction of the DNA linker patch in the lipid bilayer and with the particle surface. By considering small displacements of the particles, one can define an equivalent "translational" flexibility coefficient $D_T[\boldsymbol{\theta\theta}]$, which is linked to D_T as $D_T[\boldsymbol{\theta\theta}] = (\pi R/180\,\mathrm{deg})^{-2} D_T$. If the flexibility is dominated by translational diffusivity of the individual spheres, we can calculate its maximum magnitude from D_T. This would in turn mean that the flexibility scales with the particle radius as $1/R$, in the same way as translational diffusivity and not as $1/R^3$, as we[244] and others assumed in previous works.[107]

Indeed, using the methods explained in Section 6.2.3, for an individual sphere at a height of $(1.03^{+0.05}_{-0.02})R$ above the substrate, which corresponds to the heights of the spheres in the chains as found in the simulations, we find a translational diffusion coefficient between 0.046 and 0.071 $\mu m^2\,s^{-1}$. For comparison, the bulk diffusion coefficient of the spheres, far from the substrate, is 0.229 $\mu m^2\,s^{-1}$. Note that even a small change in the height above the substrate has a large effect on the calculated diffusion coefficient, therefore, the spread in the translational diffusion coefficient in Figure 6.15 is most likely larger than the reported spread, which is estimated from the fit of a linear model to the MSD using the method described in Section 6.2.4. In the same way, the uncertainty in the expected flexibility calculated from the translational diffusivity of an individual sphere is also large. The equivalent range of flexibilities $D_T[\boldsymbol{\theta\theta}]$ based on these values is shown in green in Figure 6.15c. Because the value of the equivalent $D_T[\boldsymbol{\theta\theta}]$ of an individual sphere is very close to the flexibilities we find in our simulations, we conclude that the maximum flexibility is indeed set by the translational diffusion coefficient of the individual spheres.

6.4 Conclusions

In conclusion, we have studied flexibly linked colloidal chains of three to six spheres using both simulations and experiments. We have analyzed their conformational free energy in several different ways. First, we found that the chains are freely-jointed, except for configurations that are forbidden because of steric restrictions due to interpenetrating particles. Furthermore, apart from some deviations because of their finite length, two-dimensional Flory theory for infinitely long polymers can describe their conformational free energy in terms of reduced end-to-end distance and radius of gyration very well. We found that the effective bending stiffness, which measures deviations from opening angles close to straight angles, scales according to the worm-like chain model.

Then, we have studied the shape-dependent short-time diffusivity of the trimer and tetramer chains. We found that the simulations can adequately model the experimental diffusion tensor of flexible trimers. For the flexibly-linked tetramers, we have

found that shape affects the short-time diffusion tensor in ways similar to what we have found for the shorter trimers. Namely, translational and rotational diffusivity are highest in directions that correspond to the lowest projected surface area, in other words, the more compact shapes, and the flexibility is highest for the more elongated shapes. Furthermore, there are nonzero couplings between translational diffusivity and both rotational diffusivity and flexibility, similar to what we found for the flexible trimers. Additionally, there is a strong negative coupling between the diffusivities of the two opening angles.

By determining the shape-averaged translational and rotational diffusivity for chains of three to six spheres, we found that these scale as function of chain length according to Kirkwood-Riseman theory. Their maximum flexibility does not depend on the length of the chain, but is determined by the near-wall in-plane translational diffusion coefficient of an individual sphere. The experimental flexibility is approximately 75 to 80 % of the flexibility calculated from the simulated data, because of friction of the DNA linker patch.

Overall, we found a good agreement between the experimental measurements and the simulations, except for translational diffusivity. In that case, we hypothesize that the difference in surface slip in the experiments, where there is a finite slip length due to the hydrogel surface, and in the simulations, where we use a no-slip boundary condition, lead to a higher translational diffusivity in the experiments. We hope our work aids the study of diffusivity of flexible objects found in complex mixtures relevant in, for example, the cosmetic, pharmaceutical and food industries, as well as in biological systems. Our findings may have implications for understanding both the diffusive behavior and the most likely conformations of macromolecular systems in biology and industry, such as polymers, single-stranded DNA and other chain-like molecules.

Acknowledgments

This chapter is based on the following publication:

Conformations and diffusion of flexibly linked colloidal chains.
R.W. Verweij, P.G. Moerman, L.P.P. Huijnen, N.E.G. Ligthart, I. Chakraborty, J. Groenewold, W.K. Kegel, A. van Blaaderen and D.J. Kraft
Journal of Physics: Materials, in press (2021). doi:10.1088/2515-7639/abf571

We thank Ali Azadbakht for the design and setup of the Optical Tweezers and his technical support. We are grateful to Aleksandar Donev and Brennan Sprinkle for fruitful discussions and for providing us with example code for the simulations. We thank Piotr Szymczak for useful discussions about the center of diffusion. The simulations were partly performed using the ALICE compute resources provided by Leiden University. J. Groenewold wishes to thank the program for Chang Jiang Scholars and Innovative Research Teams in Universities (no. IRT 17R40) and the 111 Project of the PRC. This project has received funding from the European Research Council (ERC) under the European Union's Horizon 2020 research and innovation program (grant agreement no. 758383) and from the NWO graduate program.